Use of a Reflectivity Operator Based on Double-Moment Thompson Microphysics for Direct Assimilation of Radar Reflectivity in GSI-Based Hybrid En3DVar

CHENGSI LIU,[a] HUIQI LI,[b,a] MING XUE,[a,c] YOUNGSUN JUNG,[a] JUN PARK,[a] LIANGLYU CHEN,[a,d] RONG KONG,[a] AND CHONG-CHI TONG[a]

[a] Center for Analysis and Prediction of Storms, University of Oklahoma, Norman Oklahoma
[b] Institute of Tropical and Marine Meteorology, China Meteorological Administration, Guangzhou, China
[c] School of Meteorology, University of Oklahoma, Norman Oklahoma
[d] Chongqing Institute of Meteorological Sciences, Chongqing, China

ABSTRACT: The assimilation of reflectivity (Z) within 3DVar or hybrid ensemble-3DVar (En3DVar) requires the adjoint of the Z observation operator. With the 3DVar or En3DVar method, previous studies often use Z operators consistent with a single-moment microphysics scheme even when the forecast model uses a double-moment scheme. As such, only the mixing ratios of hydrometeors are directly updated by the data assimilation (DA) system, leading to inconsistency between the analyzed microphysics state variables and the microphysics scheme in the prediction model. In this study, we formulated a Z operator consistent with the double-moment Thompson microphysics used in the numerical integrations; in the operator the snow and graupel reflectivity components are simplified using functions fitted to T-matrix simulation results. This operator and its adjoint are implemented within the GSI hybrid En3DVar DA system to enable direct assimilation of Z with a consistent operator. The impacts of this new operator on convective storm analysis through DA cycles, and on the ensuing 3-h forecasts are first examined in detail for a tornado outbreak case of 16 May 2017 in Texas and Oklahoma, and then for five additional thunderstorm cases. Forecast reflectivity, hourly precipitation, and updraft helicity tracks are subjectively evaluated, while neighborhood ETSs and performance diagrams are examined for reflectivity and/or precipitation. Compared to experiments using a Z operator consistent with a single-moment microphysics scheme, the Z operator consistent with double-moment Thompson microphysics used in the forecast model produces better forecasts of reflectivity, hourly precipitation, and updraft helicity tracks with smaller biases, and the improvement is somewhat larger for a higher Z threshold.

KEYWORDS: Radars/Radar observations; Short-range prediction; Data assimilation

1. Introduction

Successful numerical prediction of convective-scale weather requires accurate initial conditions and a prediction model with microphysical (MP) processes capable of accurately simulating deep moist convection. Bulk microphysics (BMP) is an approach that parameterizes cloud and precipitation processes by assuming semiempirical functions of the particle size distributions (PSDs), such as the Marshall–Palmer (Marshall and Palmer 1948) or gamma distribution (Ulbrich 1983) that contain two and three free parameters, respectively. With the assumptions of the functional forms of PSDs that have a limited number of free parameters, typically only a few prognostic equations are needed to uniquely determine each PSD. The kth moment of the PSD is defined as

$$M_k = \int_0^\infty N(D)D^k\,dD, \qquad (1)$$

where $N(D)$ represents the number concentration with diameters in the size range D to $D + dD$. As the equation shows, the zeroth moment M_0 of the PSD is the particle total number concentration, the third moment M_3, being the third power of diameter D, is proportional to the total mass content (e.g., the mixing ratios), and the sixth moment is linked to radar reflectivity factor. It is usually the moments of the PSDs or directly related quantities that are predicted and the number of moments that are predicted is used to name such schemes.

Single-moment (SM) BMP schemes typically predict the hydrometeor mixing ratios (e.g., Kessler 1995; Lin et al. 1983) while double-moment (DM) BMP schemes typically predict the total number concentrations of all or some of the hydrometeors in addition to the mixing ratios (e.g., Milbrandt and Yau 2005a; Thompson et al. 2004). To fully prognose all three free parameters in the gamma PSD, we need to predict three moments of the PSD, leading to three-moment or triple-moment BMP schemes where the sixth moment of PSD or radar reflectivity factor is predicted as well (e.g., Milbrandt and Yau 2005b).

Due to their relatively low cost, SM MP schemes (e.g., Hong and Lim 2006; Kessler 1995; Lin et al. 1983) have been in common use for a long time in both research and realtime forecasting applications (e.g., Kain et al. 2006; Liu and Xue 2008; Tallapragada et al. 2014). Such schemes typically assume fixed values of the intercept parameters and zero value for the shape parameter, leading to large sensitivity of simulation and prediction results to the assumed parameter

---

Jung's current affiliation: NOAA/NWS/Office of Science and Technology Integration, Silver Spring, Maryland.

Corresponding author: Ming Xue, mxue@ou.edu

values (e.g., Gilmore et al. 2004; Snook et al. 2008). By independently predicting the mixing ratios and total number concentrations of hydrometeors, DM MP schemes allow for more flexibility with the MP processes, such as changing the number concentration during aggregation or breakup while keeping the mixing ratios constant. In addition, the DM MP scheme is capable of simulating hydrometeor size sorting, which results in a more realistic hydrometeor size vertical distribution (Dawson et al. 2010; Luo et al. 2017; Luo 2018). A number of recent studies (e.g., Dawson et al. 2010; Johnson et al. 2016; Jung et al. 2010, 2012; Labriola et al. 2017; Luo et al. 2017; Luo 2018; Putnam et al. 2014) have shown that DM MP can produce more realistic convective storm structure and evolution, such as hydrometeor size sorting, polarimetric signatures and hail prediction. The Thompson MP scheme (Thompson et al. 2008) is a partially DM MP scheme, which predicts two moments to rain and cloud ice but predicts a single moment for other hydrometeor species. Within the United States, the Thompson MP scheme is used in the 13 km Rapid Refresh (RAP; Benjamin et al. 2016) and 3 km High-Resolution Rapid Refresh (HRRR; Alexander et al. 2020; Jankov et al. 2019; Smith et al. 2008) operational numerical weather prediction (NWP) systems.

In addition to MP parameterization, radar data assimilation (DA) is another key component in a successful convective-scale NWP system because radar data can provide three-dimensional observations of the internal structures of storms at high spatial and temporal resolutions and hence enable proper initialization of convective storms. Numerous studies have found that radar DA can benefit convective-scale storm analyses and forecasts (e.g., Carley 2012; Duda et al. 2019; Gao and Stensrud 2012b; Hu et al. 2006; Kong et al. 2018; Liu et al. 2020; Sun and Crook 1997; Tong and Xue 2005; Wang and Wang 2017; Xue et al. 2003; Yussouf et al. 2013). Radar reflectivity (Z) DA is more challenging than radial velocity (V_r) due to the high nonlinearity of the Z observation operator and the direct linkage of the Z measurement to precipitating hydrometeors and the associated MP processes.

To initialize a forecast using a DM MP scheme, some studies used the ensemble Kalman filter (EnKF, Evensen 2003) with a DM-based Z operator to update both hydrometeor mixing ratios and total number concentrations when assimilating radar Z. Xue et al. (2010) was among the first to estimate all state variables associated with the DM MP scheme (Milbrandt and Yau 2005a) using EnKF from Z and V_r observations in Observation System Simulation Experiments. Jung et al. (2012) found for a real supercell case that EnKF combined with a DM scheme is able to produce simulated polarimetric radar signatures that match real radar observations while with a SM scheme, the system is fundamentally incapable of simulating such signatures.

The U.S. operational forecast systems currently use the Gridpoint Statistical Interpolation (GSI; Kleist et al. 2009) DA framework which contains both EnKF and hybrid ensemble-variational (EnVar) DA capabilities. While the regional models including the North American Mesoscale (NAM) model (Wu et al. 2016) and RAP (Hu et al. 2017) are using the EnVar method, they are not yet directly assimilating radar

Z data within EnVar, but employ a cloud analysis procedure to assimilate Z (Benjamin et al. 2016).

Without involving the adjoint of observation operator (i.e., the transpose of linearized observation operator matrix), the assimilation of Z data using EnKF is more straightforward; past studies assimilating Z data using EnKF have usually used Z operators consistent with the MP scheme used in the forecast model, and in the case of DM MP scheme, number concentration beyond the mixing ratios are updated by the EnKF algorithm (e.g., Jung et al. 2012; Labriola et al. 2020; Xue et al. 2010).

A version of the Z observation operator consistent with the Thompson MP scheme was added to the GSI EnKF DA system recently. The operator follows Jung et al. (2008) where the T-matrix method is used for the scattering calculation of raindrops, and the Rayleigh scattering approximation is applied to snow and hail particles. This EnKF system has been tested with a number of convective storm cases combined with either the Weather Research and Forecasting (WRF; Skamarock et al. 2005) or Finite-Volume Cubed-Sphere Dynamical Core (FV3; Putman and Lin 2007) model run at convection-allowing resolutions (e.g., Labriola et al. 2021; Tong et al. 2020).

Compared to the EnKF method, the hybrid EnVar method that combines static and flow-dependent ensemble background error covariance offers additional flexibilities and advantages and is used at NCEP for both global and regional operational NWP systems. Recently, hybrid EnVar capabilities have been applied to convective-scale radar DA within research systems (e.g., Gao 2014; Kong et al. 2018; Wang et al. 2019), and within GSI (Tong et al. 2020). These implementations used Z operators that are consistent with SM MP schemes, however, and as such the Z operator itself is not directly linked to additional state variables such as the total number concentrations when a DM MP scheme is used. In such systems, usually only the hydrometeor mixing ratios are updated even though total number concentration also directly affects Z. In Tong et al. (2020), due to the unavailability of a Z operator consistent with the Thompson MP scheme in GSI EnVar, a Lin-type SM MP Z operator is used in GSI EnVar while the Z operator based on the Thompson MP scheme is used in GSI EnKF so that this inconsistency introduces additional error. Given that the operational RAP and HRRR and their future successors, as well as the experimental Warn-on-Forecast System (WoFS; Wheatley et al. 2015) all use DM MP schemes, Z operators consistent with the DM MP schemes used should be developed and tested within the GSI EnVar system.

The primary goal of this study is to develop a radar Z operator consistent with the Thompson microphysics scheme implemented within GSI hybrid En3DVar, and test and evaluate it for directly assimilating Z data. We first develop an approximate Thompson microphysics Z operator, in which the ice phase reflectivity components are simplified using fit functions. The impacts of using the DM Thompson-type Z operator versus the SM Lin-type operator on the analysis and prediction of storms are examined through experiments with six convective storm cases over the United States in May 2017.

A tornadic supercell case that occurred in Texas, Oklahoma, and Kansas on 16–17 May 2017 is examined in greater detail in terms of DA and forecast performance.

The rest of this paper is organized as follows. In section 2, the Z observation operators consistent with the Lin and Thompson MP schemes are introduced. Section 3 provides a brief overview of the 16–17 May 2017 storm case, and a description of DA experiments. Experiment results including objective and subjective forecast evaluations are discussed in section 4. Section 5 summarizes the results and discusses potential future work.

2. Reflectivity observation operators

a. Reflectivity observation operator for SM Lin-type microphysics scheme

The Lin et al. (1983) three-ice microphysics scheme is a popular SM scheme whose variants have been used in many studies and modeling systems (e.g., Hong and Lim 2006; Tao et al. 2003; Xue et al. 2001). The Lin MP scheme contains three precipitating hydrometeor categories, i.e., rainwater (q_r), snow (q_s), and hail (q_h). Exponential PSDs are assumed for them, which is the gamma distribution with the shape parameter assumed to be zero. The mixing ratios of the hydrometeors are predicted while intercept parameters are specified as constant values. The storm simulations are often sensitive to the choice of intercept parameter values (e.g., Snook and Xue 2008) and some studies have tried to estimate these parameters in the DA process (e.g., Tong and Xue 2008).

Based on the assumptions of the PSD and other properties including density, the radar reflectivity factors from each of the precipitating hydrometeors can be calculated. A set of such equations are given in Tong and Xue (2005), mostly based on Smith et al. (1975), and used to assimilate Z data using EnKF together with a Lin microphysics scheme. Similar formulations are also used in Dowell et al. (2011) for Z assimilation in another EnKF system. More recently, variants of such formulations are used in variational DA systems for Z assimilation (e.g., Gao and Stensrud 2012a; Kong et al. 2018; Liu et al. 2020) and implemented in GSI EnVar. In general, the reflectivity observation operator can be written as

$$Z = 10 \log_{10}(Z_e), \qquad (2)$$

where Z_e is the equivalent reflectivity factor that contains contributions from various hydrometeor species; it is defined as

$$Z_e = \frac{\lambda^4 \eta}{\pi^5 |K_w|^2}, \qquad (3)$$

where λ is the wavelength, and η is the total backscatter cross section of all scatterers per unit volume, and $|K_w|^2$ is the dielectric factor for water. With the SM Lin-type scheme, the operator for equivalent reflectivity (Z_e) contains contributions from rainwater, snow, and hail, and each is the function of the corresponding mixing ratio:

$$Z_e = Z_{er}(q_r) + Z_{es}(q_s) + Z_{eh}(q_h). \qquad (4)$$

Based on the default values of the intercept parameters of hydrometeor PSDs and the default snow and hail densities of the Lin scheme, the equivalent reflectivity factors contributed from rainwater, snow, and hail are respectively,

$$Z_{er} = 3.63 \times 10^9 \times (\rho q_r)^{1.75}, \qquad (5)$$

$$Z_{es} = \begin{cases} 9.80 \times 10^8 \times (\rho q_s)^{1.75} & T \leq 0°C \\ 4.26 \times 10^{11} \times (\rho q_s)^{1.75} & T > 0°C \end{cases}, \qquad (6)$$

$$Z_{eh} = 4.33 \times 10^{10} \times (\rho q_h)^{1.75}, \qquad (7)$$

where T is the air temperature (°C) and ρ is the air density. The default parameter values are used here for expression simplicity, but in practice, the parameter values can be set by the user. The general formulations can be found in Tong and Xue (2005) and some special treatments using these formulas for Z assimilation within a variational framework (e.g., adding a lower limit on the hydrometeor mixing ratios and assimilating radar radial wind data in a separate pass) are discussed in Liu et al. (2020).

b. Reflectivity observation operator for DM Thompson scheme

The Thompson scheme takes a DM parameterization approach for rain and cloud ice while the snow and hail/graupel processes are still parameterized using a SM approach. Now that both rainwater mixing ratio (q_r) and total number concentration (N_{tr}) are predicted, the rain component of equivalent reflectivity factor is given by

$$Z_{er} = \frac{10^{18} \times 720(\rho q_r)^2}{\pi^2 \rho_r^2 N_{tr}}, \qquad (8)$$

where ρ_r is the rainwater density.

In the Thompson scheme, the snow PSD assumes a combination of the exponential and gamma distributions and the snow density is a function of the particle diameter. To simplify the snow reflectivity formula for the tangent linear and adjoint models, we fit simulated snow reflectivity to a power-law form of snow mixing ratio. Therefore, the relation between the snow mixing ratio (q_s) and snow reflectivity (Z_s) is derived from the model output using a curve fitting (Fig. 1a), as

$$Z_s = 16.02 \, q_s^{0.56}. \qquad (9)$$

In the Thompson scheme, graupel rather than hail is included. Even though it only predicts the mixing ratio of graupel with a SM approach, the graupel intercept parameter is diagnosed as a function of graupel mixing ratio (Thompson et al. 2008). In the later implementation (the version 4.0 of WRF Model), it is modified to be a function of supercooled rainwater and graupel mixing ratio. Due to the complexity of the later relationship, we adopted the relationship in Thompson et al. (2008) and tuned two coefficients to fit the
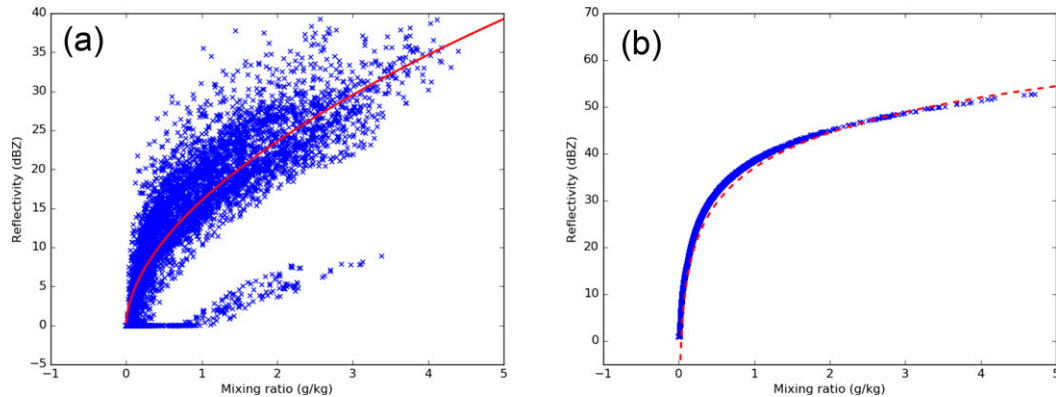
FIG. 1. Curve fitting between reflectivity and (a) snow mixing ratio and (b) graupel mixing ratio based on Thompson scheme simulation output.

simulated equivalent reflectivity (Fig. 1b). The resultant equivalent reflectivity factor for graupel is given by

$$Z_{eg} = \frac{10^{15} \times 720 \rho^{1.75} q_g^{2.5}}{\pi^{1.75} \rho_g^{1.9}}, \tag{10}$$

where ρ_g is the graupel density.

3. Overview of 16–17 May 2017 case and experiment configurations

The DA and forecast experiments using SM Lin and DM Thompson microphysics Z operators (hereafter LMP and TMP, respectively) are run for six thunderstorm cases that occurred in May 2017 over the continental United States (see list in Table 1). Overall statistical verifications are performed for these six cases. Among those cases, a tornadic supercell case that occurred over Texas, Oklahoma, and Kansas 16–17 May 2017 (Fig. 2) is selected to compare LMP and TMP in greater depth, which is a high impact and classic supercell case studied by several published papers (e.g., Chen et al. 2021; Wang et al. 2019). At approximately 1800 UTC 16 May, multiple thunderstorms were initiated along a dryline in the Texas Panhandle and moved northeastward, producing at least two weak tornados. At approximately 2100 UTC, two intense supercells were initiated and moving from near Carson County, Texas, to near Beckham County, Oklahoma. An EF-2 tornado struck Elk City, Oklahoma, around 0035 UTC, resulting in 1 fatality, 10 injuries to persons, and numerous damages to structures.

In this study, the numerical model domain has 250×250 grid points in the horizontal and 50 vertical levels and is centered on the severe weather event location for each case, following the configuration of the NSSL Experimental WoFS (Wheatley et al. 2015). The horizontal grid spacing is at 3 km. Forecasts are run using the version 3.8.1 of WRF Model. The following physics schemes are used in the experiments: the Thompson microphysics, Yonsei University (YSU) planetary boundary layer (Hong et al. 2006), RRTMG shortwave and longwave schemes (Iacono et al. 2008), and the unified Noah land surface model (Chen and Dudhia 2001). It should be noted that the Thompson MP scheme is used for all the model forecasts, i.e., during the forward integration of both the cycled DA and the free forecast.

The cycled DA and forecast experiments are described as follows (see also Fig. 3). GSI EnKF and hybrid En3DVar DA cycles are performed in a one-way coupling mode, where ensemble perturbations provided to the hybrid En3DVar are updated by EnKF but the deterministic En3DVar analysis is not used to re-center the ensemble mean EnKF analysis. For relatively short DA periods, the EnKF and En3DVar in one-way coupled mode usually do not diverge significantly, and one-way coupling ensures that the ensemble perturbations used in all En3DVar experiments are the same, and are not affected by the particular Z operator used in the En3DVar experiments (Kong et al. 2018). Following the NSSL WoFS (Skinner et al. 2018), the ensemble initial conditions of the EnKF system are taken from the 1-h High-Resolution Rapid Refresh Ensemble (HRRRE; Dowell et al. 2016) forecasts (valid at 1800 UTC) initialized at 1700 UTC. The boundary

TABLE 1. List of selected cases. Primary states affected and brief descriptions of convective mode are also provided.

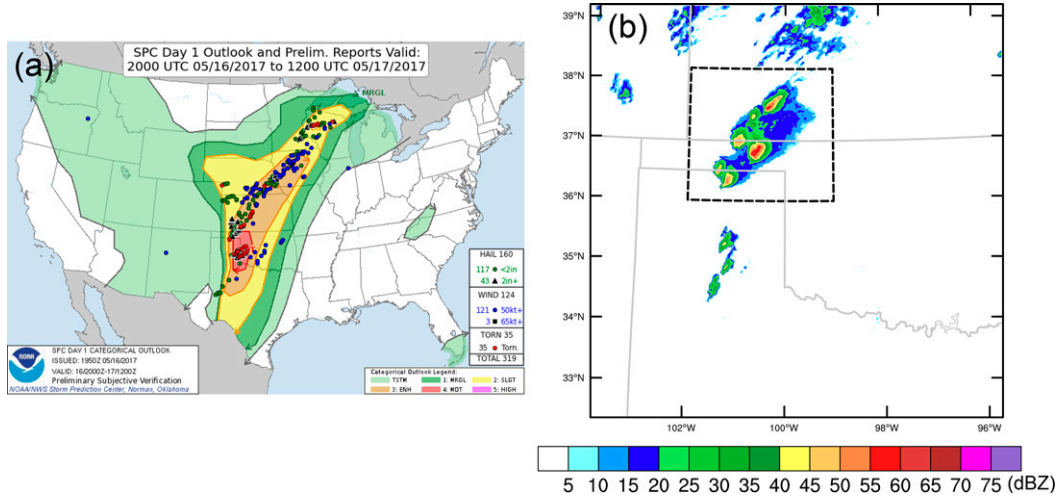| Date	Primary states affected	Event description
9 May	NM, TX	Supercell outbreak
16 May	KS, OK, TX	Discrete tornadic supercells
17 May	IA, IL, MN, WI	Mixed clusters of cells and lines
18 May	KS, OK, TX	Tornadic supercells
23 May	TX	High wind producing mixed-mode convection
27 May	AR, MO, OK	Mixed-mode convection

FIG. 2. (a) Storm reports for 16 May 2017 extracted from Storm Prediction Center (SPC). (b) Composite reflectivity at 2000 UTC 16 May 2017. The dashed black rectangle encloses the area shown in Fig. 6.

conditions are taken from HRRRE forecasts issued at 1500 UTC. The deterministic initial and boundary conditions for hybrid En3DVar are taken from the ensemble mean of EnKF initial conditions and boundary conditions, respectively. In all EnKF experiments, the Z operator consistent with Thompson microphysics is used, while in the En3DVar experiments, Z operators consistent with Lin and Thompson microphysics are used in two sets of experiments for comparison purposes.

The DA window is from 1800 to 2100 UTC (Fig. 3b). Conventional data (e.g., surface stations, buoys, soundings), radar Z and radial velocity observations are assimilated. Radar Z observations are interpolated from the grid Multi-Radar Multi-Sensor (MRMS; Smith et al. 2016) dataset to the locations of the model grid columns horizontally but remain on the 33 MRMS vertical levels. Radial velocity V_r observations are processed from the WSR-88D Level-2 data using a quality control and processing procedure from the Advanced Regional Prediction System (Brewster et al. 2005). The V_r data are interpolated to the model grid column locations horizontally but kept on the radar elevation levels in the vertical for each radar site. No further data thinning on the model

grid is employed here. Radar Z and radial velocity observations are assimilated every 15 min and conventional observations are assimilated hourly (see Fig. 3b). Free forecasts initialized from the final analyses at 2100 UTC are run for 3 h. The 3-h forecasts are performed because the motivation of the WoFS is improving short-term (0–3 h) forecasts for severe thunderstorms and their hazards (Stensrud et al. 2009; Wheatley et al. 2015).

To help alleviate problems associated with the highly nonlinear Z operator, following Chen et al. (2021), a nonlinear power transform is applied to hydrometeor mixing ratios with the power parameter p set to 0.4 in all hybrid En3DVar experiments. A 20% static background error covariance is used for hybrid En3DVar following Chen et al. (2022). In variational algorithms, nonlinear observation operators are usually linearized and an outer-loop procedure is used to reduce the impact of linearization approximation (Courtier et al. 1994). Four outer loops are used with up to one hundred iterations for the inner loop of the cost function minimization. The convergence criterion is set as 10^{-10} for the norm of the cost function gradient.

4. Results of experiments

a. Evaluations with the 16 May 2017 case

1) RESULTS OF SINGLE-TIME ANALYSES FOR THE 16 MAY 2017 CASE

To clearly show the direct impact of DA using Lin- and Thompson-based Z operators, we perform single-time hybrid En3DVar analyses at 2000 UTC using the same background from a 30-min forecast from TMP cycled DA with 30-min radar DA intervals (Fig. 3a). Specifically, during the cycled DA procedure to generate the background, the Thompson-based Z operator is used in analysis process and the Thompson MP scheme is used for the forward integration. This analysis time (2000 UTC) is chosen because several well-
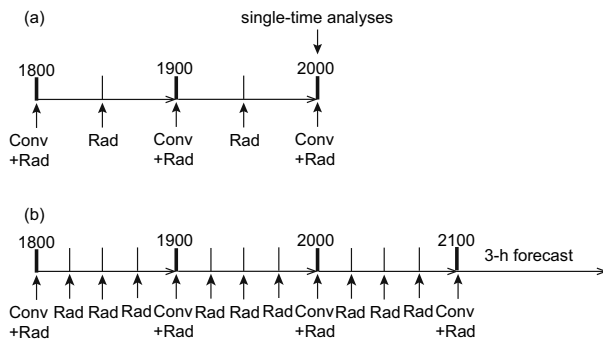

FIG. 3. The flowchart of (a) the single-time analyses and (b) the cycled data assimilation and 3-h forecast experiments.
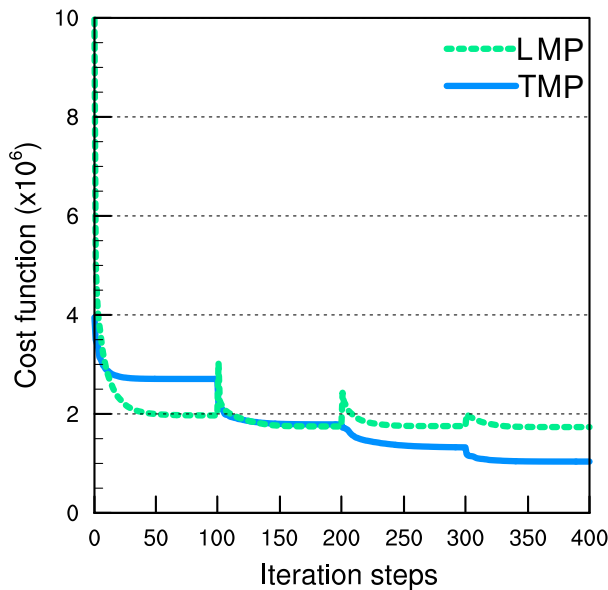
FIG. 4. Cost function with respect to number of iterations accumulated in four outer loops for the one-time analysis experiments with TMP and LMP operators at 2000 UTC 16 May 2017.

FIG. 5. Radar reflectivity RMSI (dBZ) of the background and the analysis of LMP and TMP experiments. Label "LMP_TMP" indicates that the reflectivity is calculated using the TMP Z operator.

developed storms were observed but the model predicted much weaker storms at that time, which is a suitable situation for the comparison of the analyzed reflectivity using the Lin- and Thompson-based Z operators.

To compare the convergence rates of LMP and TMP experiments, cost function values as a function of the number of iterations accumulated in the four outer loops are plotted in Fig. 4. With the Lin-based Z operator, the cost function is reduced rather quickly within the first 25 iterations within each outer iteration but there is a major jump in the cost function value at the beginning of the outer loops. This should be related to the fact that with the LMP operator, N_{tr} is not updated by the analysis, resulting in inconsistency between the mixing ratio and number concentration when the operator is relinearized around an updated state at the beginning of outer loops. Also, the cost function in LMP does not decrease much further in the later outer iterations (Fig. 4). With the Thompson-based Z operator, the cost function does not decrease as fast with inner-loop iterations, especially within the first outer loop but the reduction remains large and fast near the beginning of the second outer loop, and the reduction continues through the fourth outer loop; at the end of all iterations, the cost function in TMP is about half that of LMP. The slower initial reduction should be due to the need to adjust both mixing ratio and total number concentration but the end result is more consistent with MP states.

The root-mean-square innovations (RMSIs) of the background and analyzed reflectivity from LMP and TMP experiments are calculated using the Thompson Z operator for all grid points where the observed or analyzed reflectivity is greater than 15 dBZ (Fig. 5). For LMP experiment, the background and analyzed reflectivity are calculated by the Lin Z operator. We also calculate the background reflectivity and
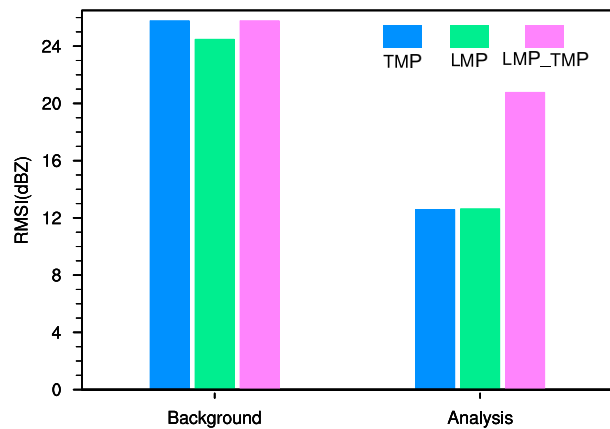
LMP-analyzed reflectivity using the TMP Z operator (labeled LMP_TMP in Figs. 5–8). The analysis RMSIs of LMP and TMP are very similar (~12 dBZ) and much smaller than that of background (~26 dBZ), indicating that both LMP and TMP are able to achieve a good fit of the analyzed reflectivity to observations, as long as the same operator is used within the cost function and for RMSI calculations. However, the mismatch between the operator within the DA cost function and the microphysics used means, to say the least, significant adjustment between the rainwater mixing ratio and number concentration once the forecast starts. In fact, when the Thompson Z operator is used to calculate the RMSI of LMP analysis, the RMSI of LMP_TMP is much higher at ~21 dBZ, even though it is lower than the background value of ~26 dBZ.

The composite reflectivity at 2000 UTC from the background and the single-time analyses of LMP and TMP are compared against observations in Fig. 6 within the dashed box domain in Fig. 2b, which is the most active convective area at that time. The observed composite reflectivity (Fig. 6a) shows that multiple supercells are well developed while the background Z calculated using the Lin and Thompson Z operators is clearly much weaker (Figs. 6b,c). As described at the beginning of this section, the background is from the 30-min forecast (Fig. 3a), during which these storms develop slowly in the model. Both of LMP and TMP experiments produce analyzed composite Z (Figs. 6e,f) very similar to observed Z (Fig. 6a) except that the intensity of the reflectivity cores is somewhat weaker. However, when calculating Z from the LMP-analyzed MP state using the Thompson Z operator (LMP_TMP), the analyzed Z generally appears much weaker than the observations, except that at the strongest reflectivity core (Fig. 6d). In a sense, this reflectivity (Fig. 6d) is what the WRF model would output at the initial time.

Cross sections taken through the vertical velocity core and extending northwestward into weaker observed reflectivity region (dashed line in Fig. 6) are analyzed to examine the impact of Z assimilation in LMP and TMP (Fig. 7). The
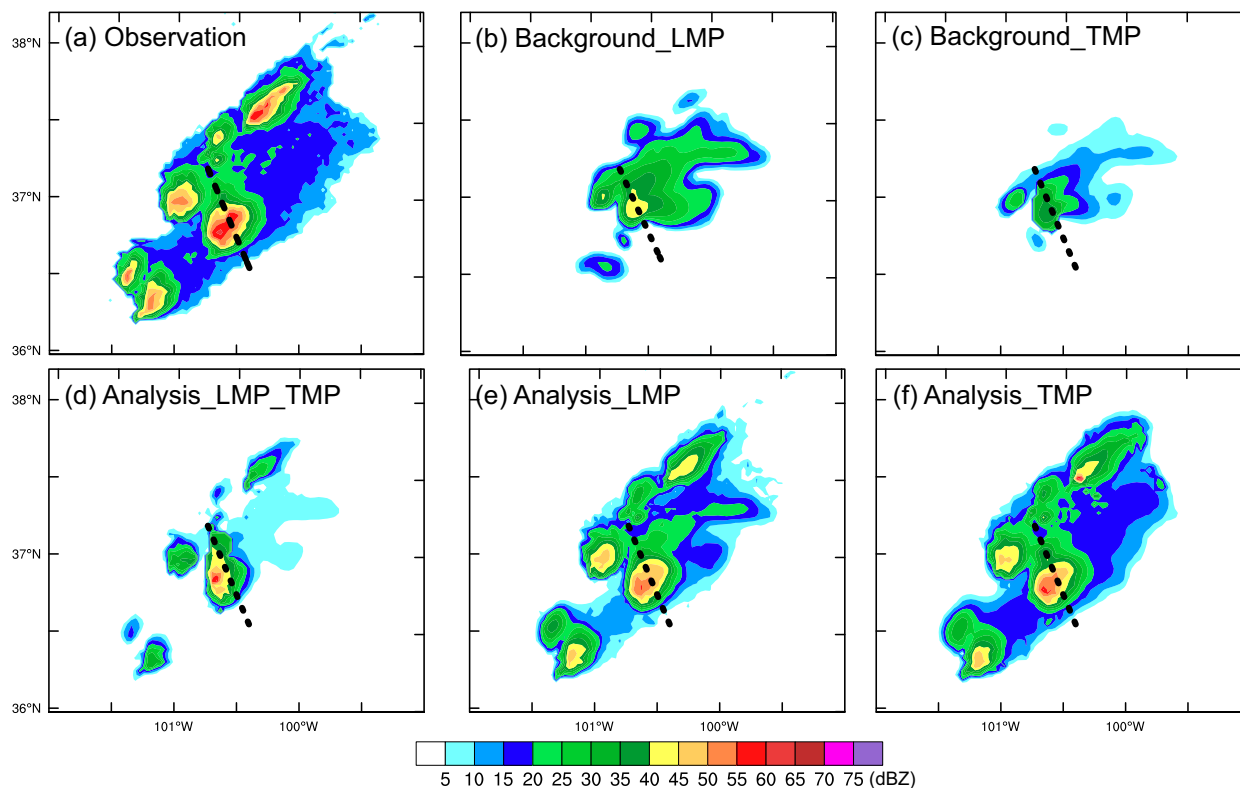
FIG. 6. Composite reflectivity (dBZ) at 2000 UTC from observations, background, and analyses of LMP_TMP, LMP, and TMP. The black dashed line in each panel indicates the location of vertical cross sections shown in Figs. 7 and 8.

background Z calculated using Lin or Thompson Z operator (Figs. 7b,c) has smaller spatial coverage than observations (Fig. 7a) and the echo top is ~8 km lower than the observed (Fig. 7a). Contrasting background Z intensities are found below and above the melting level (~4 km) with the two calculations (Figs. 7b,c), which will be further investigated and discussed later by examining the contributions to reflectivity by different hydrometeors. The analyzed Z of LMP and TMP (Figs. 7e,f) is greatly improved over the background in both cases even though the reflectivity cores are weaker than the observed as seen in composite Z. The Z calculated using the Thompson Z operator from the LMP-analyzed state (Fig. 7d) is much weaker, again as seen before in composite Z, but the calculated Z near the surface is actually higher than that calculated using Lin Z operator (Fig. 7e).

Figure 8 shows the hydrometeor mixing ratios and N_{tr} of background and single-time analyses at 2000 UTC, and the corresponding contributions to reflectivity. The contributions of rainwater (Z_r), snow (Z_s), and graupel (Z_g) are defined as the logarithmic reflectivity from the individual hydrometeors in dBZ, e.g., $Z_r = 10\log_{10}(Z_{er})$. For the background, the Thompson Z operator produces higher Z_r but lower Z_s and Z_g than the Lin Z operator. The same is seen with the analysis of LMP experiment; when the TMP operator is applied to the LMP analysis, higher Z_r but lower Z_s and Z_g are produced. This indicates that the use of the Lin Z operator in the DA system would tend to produce more (overestimated)

rainwater and less (underestimated) snow and hail/graupel in the analyses than when the Thompson Z operator is used. This explains the overestimated reflectivity near the surface in Fig. 7d when TMP operator is used to calculate Z from the LMP analysis.

Figure 8 also shows that the LMP experiment does not change N_{tr} in the background (Figs. 8a–d) while the TMP experiment does (Fig. 8e); the N_{tr} is increased in the TMP experiment within the convective region (Fig. 8e) since N_{tr} is a control variable which is the variable that directly appears in the cost function and is adjusted (controlled) by variational minimization. Both Z_r and q_r in TMP are enhanced at the high levels while the low-level spurious Z_r existing in LMP (Fig. 8c) is greatly reduced in TMP. In both LMP and TMP experiments, graupel contributes most to the analyzed Z, and the analyzed Z_g intensities in the two experiments are similar (Figs. 8i,j) and much stronger than the background Z_g. However, LMP apparently produces much lower q_g than TMP; this is again because the TMP operator produces much weaker Z_g than the LMP operator from the same state (Fig. 8h). This is directly related to the fact that q_g has a smaller exponent in the LMP operator [Eq. (7)], than in the TMP operator [Eq. (10)]. For snow, TMP produces higher q_s values, mostly at the high levels (Fig. 8o) although the difference is much smaller than for graupel.

Since En3DVar can update nonhydrometeor variables through ensemble-based cross-covariance when assimilating
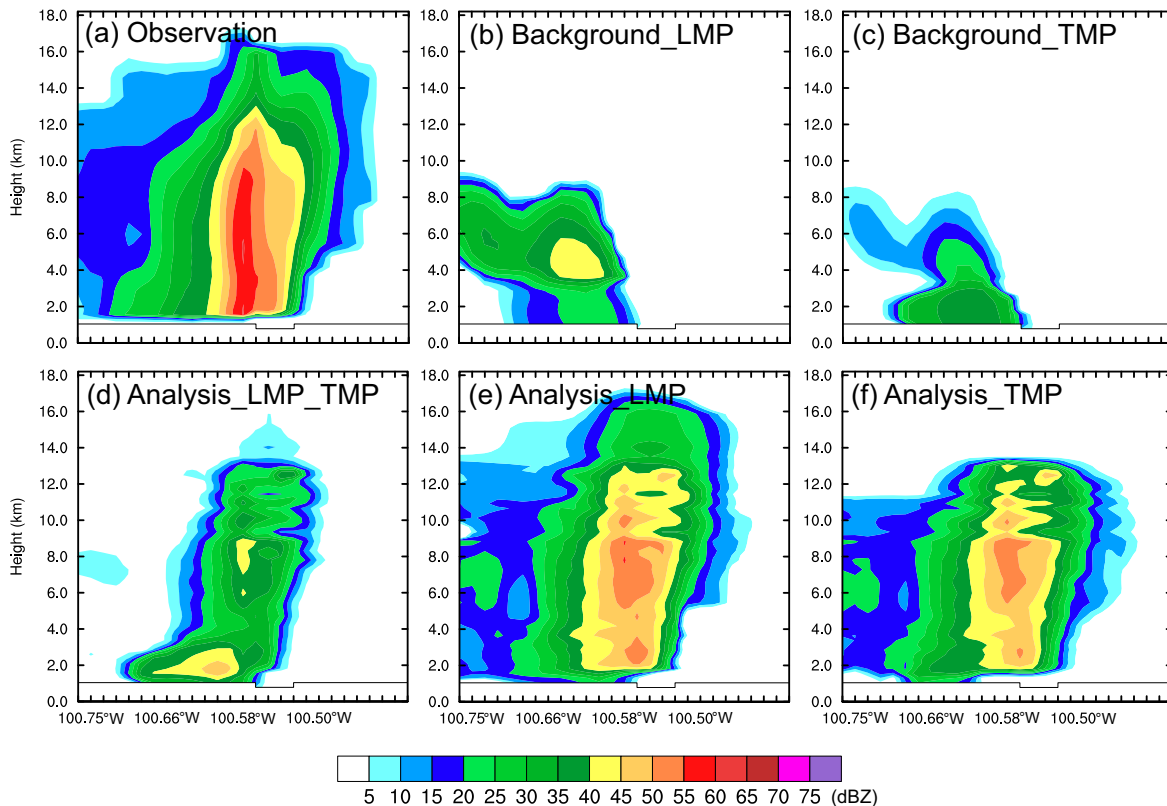
FIG. 7. Vertical cross sections along the line given in Fig. 6 of reflectivity from observations, background, and analyses of LMP_TMP, LMP, and TMP.

radar reflectivity, the impacts of DA using LMP and TMP Z operators on the analysis of kinematic and thermodynamic characteristics are examined. Figure 9 shows the analyzed near-surface potential temperature increment and maximum vertical velocity fields from the two experiments. Compared to the LMP experiment, the TMP experiment produces larger negative potential temperature increments underneath the main storm and stronger storm updrafts, which apparently help sustain the analyzed storms in the model forecast.

In summary, when the Lin Z operator is used in the variational DA, q_r and q_g tend to be overestimated and underestimated, respectively, compared to the consistent Thompson Z operator is used, while the background N_{tr} cannot be directly updated by variational DA through the observation operator.

2) RESULTS OF 3-H CYCLED ANALYSES AND 3-H FORECASTS FOR THE 16 MAY 2017 CASE

In this subsection, we examine the final analyses using the two operators for 15-min assimilation cycles during the 3-h assimilation period from 1800 to 2100 UTC, followed by a 3-h free forecast period, as depicted in Fig. 3b. At the end of DA cycles at 2100 UTC, the observed reflectivity objects (composite $Z > 45$ dBZ) are captured quite well by both LMP and TMP experiments (Figs. 10b,c). However, the reflectivity cores are somewhat overestimated and the stratiform reflectivity is substantially underestimated in the LMP experiment

(Fig. 10b). The intensity and coverage of analyzed Z in the TMP experiment (Fig. 10c) are closer to observations especially with the weak echo regions, except for some spurious echoes in the Texas Panhandle. For the 3-h forecast, LMP fails to predict the tornadic supercell near Elk City, Oklahoma, and has eastward and southeastward displacement errors for northernmost and southernmost supercell in Oklahoma, respectively (Fig. 10e). TMP also has similar displacement errors but more successfully predicts the tornadic supercell near Elk City even though with eastward displacement errors (Fig. 10f). In Kansas, LMP produces more scattered, spurious storm cells than TMP.

To quantitatively compare forecasts of the two experiments, neighborhood equitable threat scores (NETS, Clark et al. 2010) for low (20 dBZ) and high (45 dBZ) thresholds are shown in Figs. 11a,b, respectively. The neighborhood radius is set to 40 km, following Skinner et al. (2018) who used it for verification of convective scale forecasts of the WoF system. For the 20-dBZ threshold, TMP has better skill in the first 90 min because the low reflectivity is substantially underestimated in the LMP analysis (Fig. 10b). TMP is overtaken somewhat by LMP from 90 to 135 min and the scores become similar in the last 45 min. For the 45-dBZ threshold, TMP is superior during almost the entire forecast period except for the first 30 min when its score is slightly lower, possibly due to its having more spurious >45-dBZ echoes (Fig. 10c).
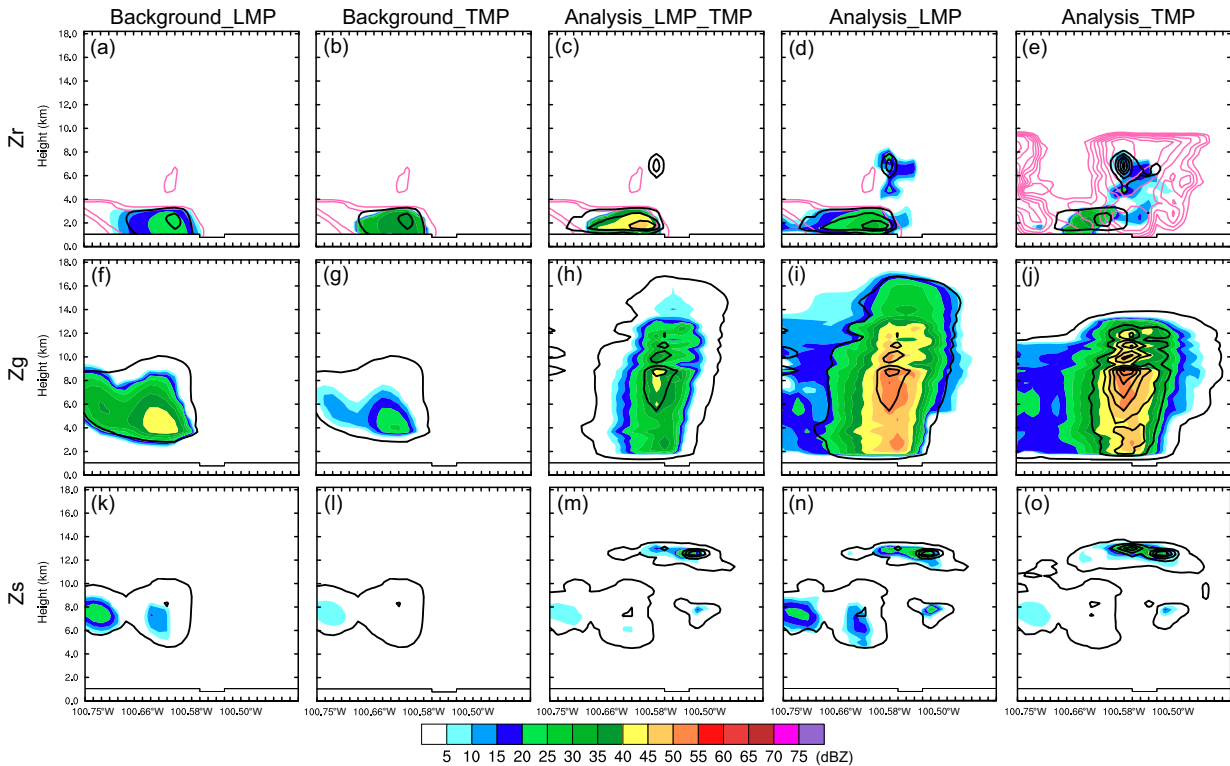
FIG. 8. Vertical cross sections along the line given in Fig. 6 of reflectivity components (shading) from different hydrometeors and corresponding mixing ratios and N_{tr} (contours) at 2000 UTC from background [using (a),(f),(k) LMP operator and (b),(g),(l) TMP operator] and analyses (together with Z components from LMP and TMP experiments. LMP_TMP calculates Z components using TMP operator). (top) Rainwater mixing ratio (contoured in black starting at 0.01 g kg^{-1} at intervals of 0.5 g kg^{-1}) and total number concentration [magenta contours of $\log_{10}(N_{tr})$ starting at 1 m^{-3} at intervals of 0.5 m^{-3}]; (middle) graupel mixing ratio (contoured starting at 0.01 g kg^{-1} at intervals of 0.5 g kg^{-1}); and (bottom) snow mixing ratio (contoured starting at 0.01 g kg^{-1} at intervals of 0.5 g kg^{-1}).

Contingency table based verification indices including bias, probability of detection (POD), false alarm ratio (FAR), and critical success index (CSI) of composite reflectivity forecasts for the same two thresholds are presented in performance diagrams (Roebber 2009, Figs. 11c,d). For the 20 dBZ threshold, TMP has moderately higher PODs and less bias in the 1- and 3-h forecasts but lower POD and larger low-bias in 2-h forecast compared to LMP experiment. For the 45-dBZ threshold, TMP has much higher CSIs than LMP but similar biases for the 1- and 2-h forecasts while for the 2-h forecasts the difference is smaller and the bias of TMP is slightly larger. Overall, in terms of the NETS and performance diagram, TMP has better (comparable) performance for the high (low) reflectivity forecasts than LMP.

Radar data assimilation mainly affects the analysis of storm interior structure and tends to make little direct impact on the storm environment. In this study, we found that the biggest differences between LMP and TMP experiments are at the low levels associated with the cold pool. This is not surprising given that cold pool is sensitive to microphysics processes through, e.g., evaporative cooling and water loading, while the reflectivity operators affects analyzed hydrometeors directly. The cold pool strength affects the gust front convergence lifting thereby storm evolution. The analyzed potential

temperature at the lowest model level and maximum vertical velocity at the end of the DA cycles (i.e., 2100 UTC) are compared in Fig. 12. The cold pool and the updraft near area "A" are notably stronger in the TMP experiment than that in the LMP experiment; which appears to have led to the stronger predicted storms in Kansas (Fig. 10f). In area "B," even though a clear cold pool is not produced in either experiment, the updraft in the LMP experiment is much weaker than in the TMP experiment, so that the southernmost storm dies out around 2345 UTC, resulting in the unsuccessful prediction of the Elk City supercell (Fig. 10e).

The predicted hourly precipitation for the first (2100–2200 UTC 16 May) and last (2300 UTC 16 May–0000 UTC 17 May) forecast hour verified against observations derived from MRMS are shown in Fig. 13. In the first forecast hour, LMP fails to predict the northernmost rainband 1 and exhibits westward bias for the rainband 2 near the Oklahoma–Kansas border (Fig. 13b). TMP more accurately predicts the locations of both rainbands but the rainband intensities are underestimated (Fig. 13c). Both experiments successfully predict the northern precipitation center 3 in Texas Panhandle but underpredict the southern precipitation center 4 with southeastward displacement. In the last forecast hour, LMP fails to predict the two main areas of precipitation (5 and 6) in Kansas
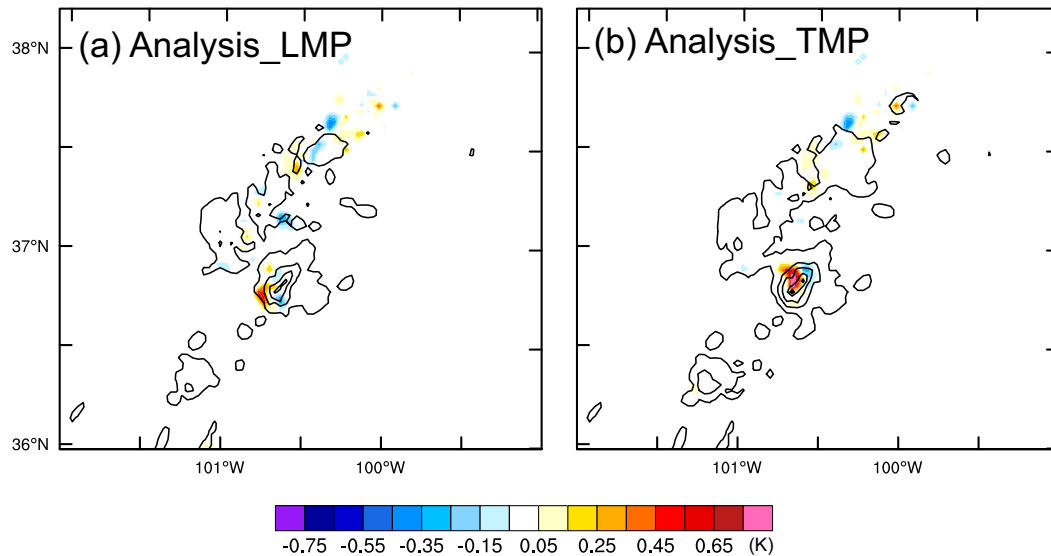
FIG. 9. Potential temperature increments (shading, K) at the lowest model level and maximum vertical velocity (contoured starting at 1 m s^{-1} at intervals of 5 m s^{-1}) at 2000 UTC from the analyses of (a) LMP and (b) TMP experiments.

(Fig. 13e) while TMP captures the southern one (6) much better (Fig. 13f). For the three precipitation bands in western Oklahoma, both experiments capture the northernmost one (7) with somewhat northeastward bias. LMP mostly misses the two southern bands (8 and 9) while TMP produces one band that is displaced to the southeast of the middle band 8 (Fig. 13f).

The NETS and performance diagram of hourly precipitation at the threshold of 10 mm of the two experiments are plotted in Fig. 14. The NETS of LMP of the first hour is much lower than that of TMP and remains lower in the second and third hour of forecast, and such differences are much larger than those of forecast reflectivity shown in Fig. 11, indicating the benefit of using the TMP Z operator goes beyond simply improving the microphysical states. The NETS difference between LMP and TMP becomes smaller with longer forecast time as the impact of initial conditions tend to decrease with forecast time when the underlying forecast model is the same. The grouping of CSI within the performance diagram generally matches the NETS results, indicating again the TMP performs much better than LMP for precipitation prediction at the first hour. In terms of bias scores, underprediction is seen for both experiments but the bias of TMP is smaller, especially for the first and second hour.

Updraft helicity (UH) (Kain et al. 2008) can be used to detect mesocyclones in convection-allowing model forecasts, and serve as a surrogate predictor of severe weather including tornados (e.g., Clark et al. 2012). To examine the impact of LMP and TMP operators on tornadic storm forecasts, the instantaneous UH in the 2–5-km layers AGL based on the 0–3-h forecast output every 5 min is evaluated. The UH tracks aggregated over the 3 h are overlaid with Storm Prediction Center (SPC) tornado reports in Fig. 15. Compared to LMP,

the northernmost UH track predicted by TMP in Kansas is more consistent with tornado reports. Both experiments successfully predict the northern UH track over the Texas–Oklahoma border. LMP does not predict the southernmost UH track associated with the Elk City tornado as it fails to predict the tornadic supercell near Elk City (Fig. 10e) whereas TMP predicts a very week UH track with a southward displacement.

b. *Quantitative verifications for six cases*

To quantitatively evaluate the LMP and TMP performance for multiple severe thunderstorm cases briefly described in section 3, the RMSIs of LMP and TMP for 3-h forecast reflectivity for all the six cases are compared in Fig. 16. Overall, there is consistent improvement across all the cases. Specifically, except for the 9 and 23 May cases, the RMSIs of TMP are lower than those of LMP during the entire 3-h forecast for the other cases (Figs. 16b,c,d, and f). As for the 9 and 23 May cases, the differences in the RMSIs between TMP and LMP are small (Figs. 16a,e). The RMSIs of TMP averaged over six cases are about 0.5 dBZ lower than those of LMP during the entire 3-h forecast (Fig. 16g).

NETS and performance diagram of LMP and TMP at thresholds of 20 and 45 dBZ are compared in Fig. 17. For the 20-dBZ threshold, the NETS of TMP is 0.08 higher than that of LMP for 15-min forecast, and then their difference gradually decreases with forecast time but remains at about 0.03 at 3 h of forecast (Fig. 17a). For the 45-dBZ threshold (Fig. 17b), the NETS of TMP is generally ~0.05 higher than that of LMP at most forecast times but the difference is increased to 0.09 (0.75 for TMP and 0.66 for LMP) at 3 h of forecast, suggesting that the benefit of using the TMP Z operator consistent with the Thompson MP scheme in the forecast
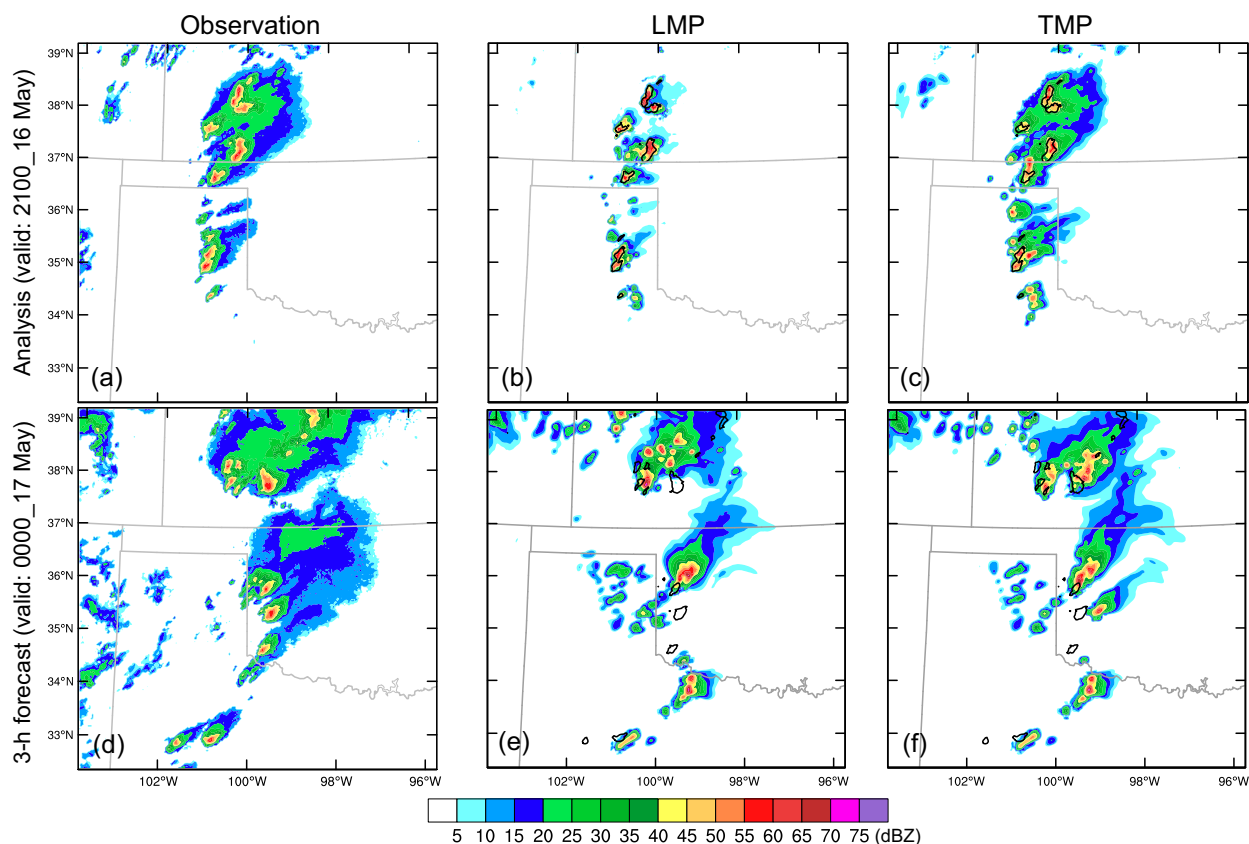
FIG. 10. Composite reflectivity (dBZ) at (top) 2100 UTC 16 May and (bottom) 0000 UTC 17 May from (a),(d) observations; (b),(e) LMP; and (c),(f) TMP experiments. Note that (b) and (c) are analyses and (e) and (f) are forecasts. The observed 45-dBZ contours are overlaid in the experimental analyses and forecasts.

model can be sustained for 3 h of forecast, and more so for the higher Z threshold corresponding to more intense convection. Given that the NETS scores in Fig. 17 are averaged over six cases, the conclusions are more robust than those for a single case presented earlier; for the 16 May case, the improvement in NETS with TMP is not seen at all forecast times and for both thresholds but it is true for the six-case average. The statistical significance of the scores are also examined using a bootstrap resampling method with replacement to generate 1000 realizations. The scores from the six cases are randomly selected 1000 times, and for these samples, the average and two-tailed 90% confidence interval are calculated (Hamill et al. 2011; Xue et al. 2013; Pan et al. 2014). The same technique is also applied to the differences in the scores between the LMP and TMP experiments to determine whether the improvement of the TMP operator over the LMP operator is statistically significant. At most forecast lead times, the 90% confidence intervals of the NETSs of the LMP and TMP experiments overlap (Figs. 17a,b), and the confidence intervals of the differences (TMP-LMP) include zero except for 15 min for the 20-dBZ threshold (Fig. 17c) and 180 min for the 45-dBZ threshold (Fig. 17d), indicating that the improvement is statistically insignificant. However, it should be noted that while producing statistically significant improvement is

desirable, the difference is not expected to be as large as, e.g., assimilating radar data or not, and even if statistically insignificant improvement still supports the TMP operator as the preferred choice.

Seen from the performance diagrams, the Z forecasts of both LMP and TMP are nearly unbiased for the 20-dBZ threshold (Fig. 17e) but there are overprediction biases of 1.1–1.2 for the 45-dBZ threshold (Fig. 17f), likely the results of spurious cells of significant intensity in the prediction. The CSIs of TMP are only slightly higher than those of LMP for the 20-dBZ threshold (Fig. 17e) but the superiority is larger for the 45-dBZ threshold (0.76–0.81 versus 0.65 and 0.78), consistent with the NETSs. The performance diagrams indicate that the better NETSs of TMP experiment are not due to higher biases; in fact, TMP yields slightly smaller positive biases.

5. Summary and conclusions

Within the variational DA framework, the assimilation of radar reflectivity Z requires the implementation of the reflectivity observation operator and its adjoint within the cost function. Z operators consistent with SM MP schemes (e.g., Lin microphysics) are typically used in earlier studies even
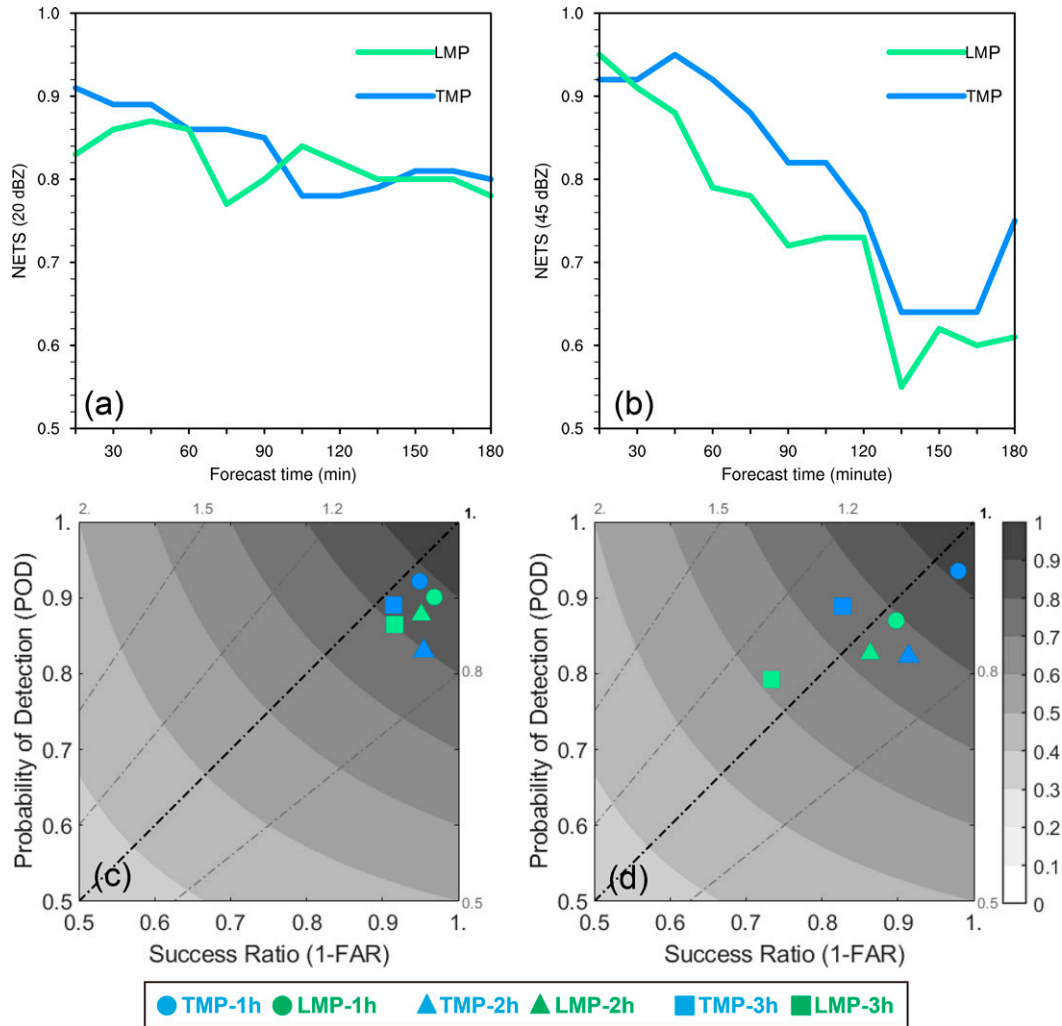
FIG. 11. (a),(b) NETS and (c),(d) performance diagram for composite reflectivity forecasts of LMP (green) and TMP (blue) experiments with thresholds of (left) 20 and (right) 45 dBZ. Diagonal and curved lines in (c) and (d) represent lines of constant BIAS and CSI, respectively. Dot, triangle, and rectangle marks in (c) and (d) represent 1-, 2-, and 3-h forecasts, respectively.

when the forecast model uses a DM MP scheme, such as the Thompson MP scheme that is employed within the operational HRRR. Because SM schemes predict only hydrometeor mixing ratios, the variational DA system using the SM Z operator usually only updates the mixing ratios without the total number concentrations that are also predicted by a DM MP scheme, resulting in inadequate initialization of the MP state variables that can degrade the subsequent forecast. In this study, we implement a Z operator consistent with the Thompson microphysics together with its adjoint within the hybrid GSI En3DVar system for direct assimilation of Z. The performance of the TMP operator is compared with an operator consistent with the SM Lin MP scheme.

DA and forecast experiments using LMP and TMP operators are first compared in greater detail for a tornadic supercell case that occurred in Texas, Oklahoma, and Kansas on 16–17 May 2017. With the mismatch between the Thompson

MP in the forecast model and the LMP operator, the variational DA using LMP operator produces overestimated rainwater mixing ratio and underestimated snow and hail mixing ratios. In addition, the background rainwater total number concentration (N_{tr}) cannot be updated with the LMP operator. This mismatch problem in the LMP experiment leads to worse performance in early hour forecast of reflectivity and precipitation than the TMP experiment. Furthermore, the fatal tornadic supercell near Elk City, Oklahoma, is not successfully initiated in the LMP experiment; the improper analyses of hydrometeors and N_{tr} appear to be the reason. In the TMP experiment, this tornadic supercell is more successfully predicted even though with eastward displacement errors.

The hybrid DA system based on the LMP and TMP operators are further applied to five additional cases from May 2017, using the same 3-h cycled DA procedure. Reflectivity
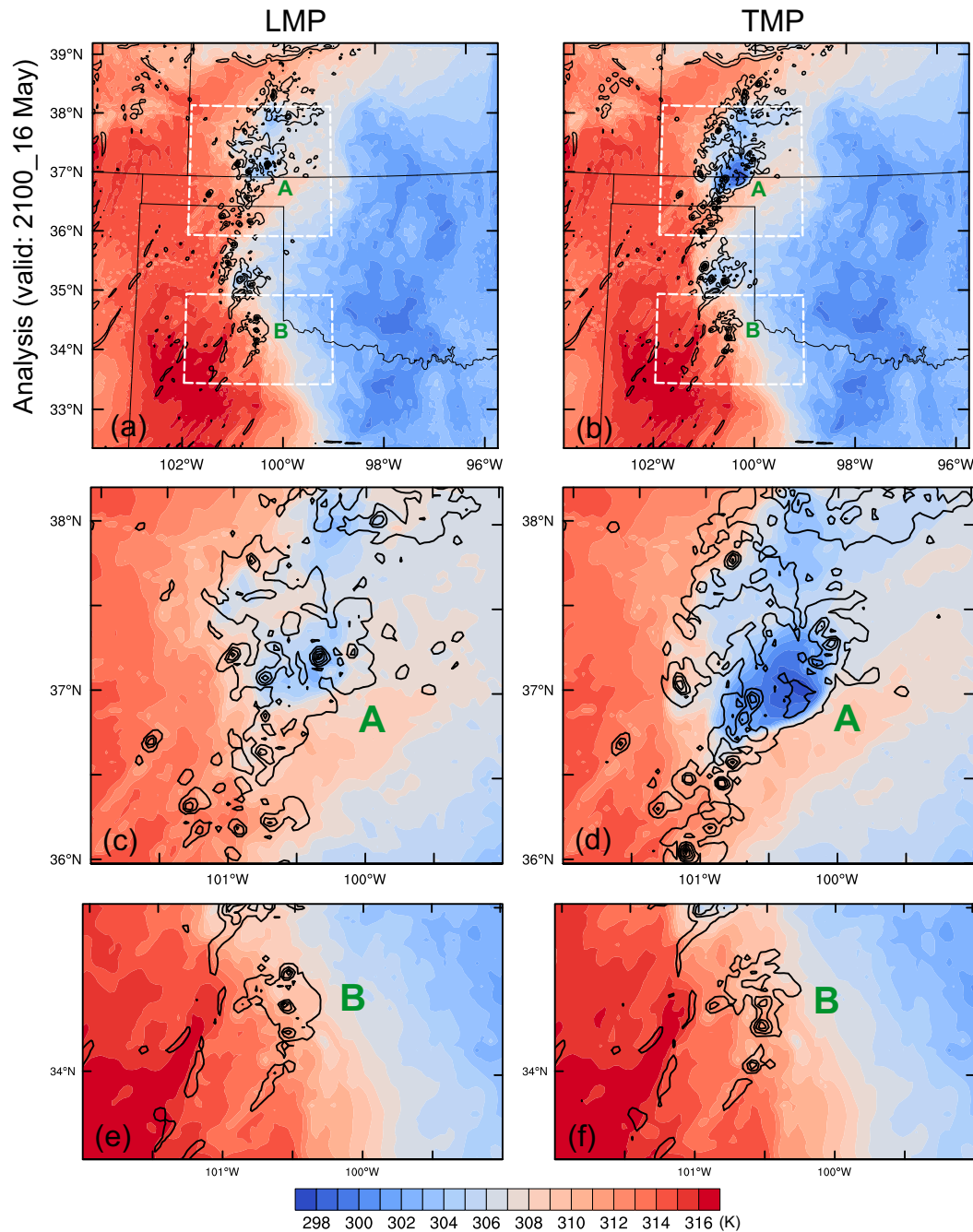
LMP

TMP

FIG. 12. Potential temperature (shading, K) at the lowest model level and maximum vertical velocity (contoured starting at 1 m s^{-1} at intervals of 5 m s^{-1}) at 2100 UTC 16 May from the (a) LMP and (b) TMP experiments. Letters "A" and "B" label the convective areas mentioned in the text. (c),(d) The enlarged images of the dashed white rectangles enclosing "A" in (a) and (b), respectively. (e),(f) The enlarged images of the dashed white rectangles enclosing "B" in (a) and (b), respectively.

forecasts up to 3 h are quantitatively evaluated in terms of the RMSI, NETS and performance diagram. Compared to LMP, the RMSI of TMP is about 0.5 dBZ lower through the 3 h of forecast. In terms of NETS and performance diagram at thresholds of 20 and 45 dBZ, TMP produces better reflectivity

forecast than LMP, especially for reflectivity over 45 dBZ, suggesting that using a radar Z operator consistent with the MP scheme of the forecast model is more important for more intense convection. While some potential benefits provided by the TMP operator are indicated in this study, evaluations
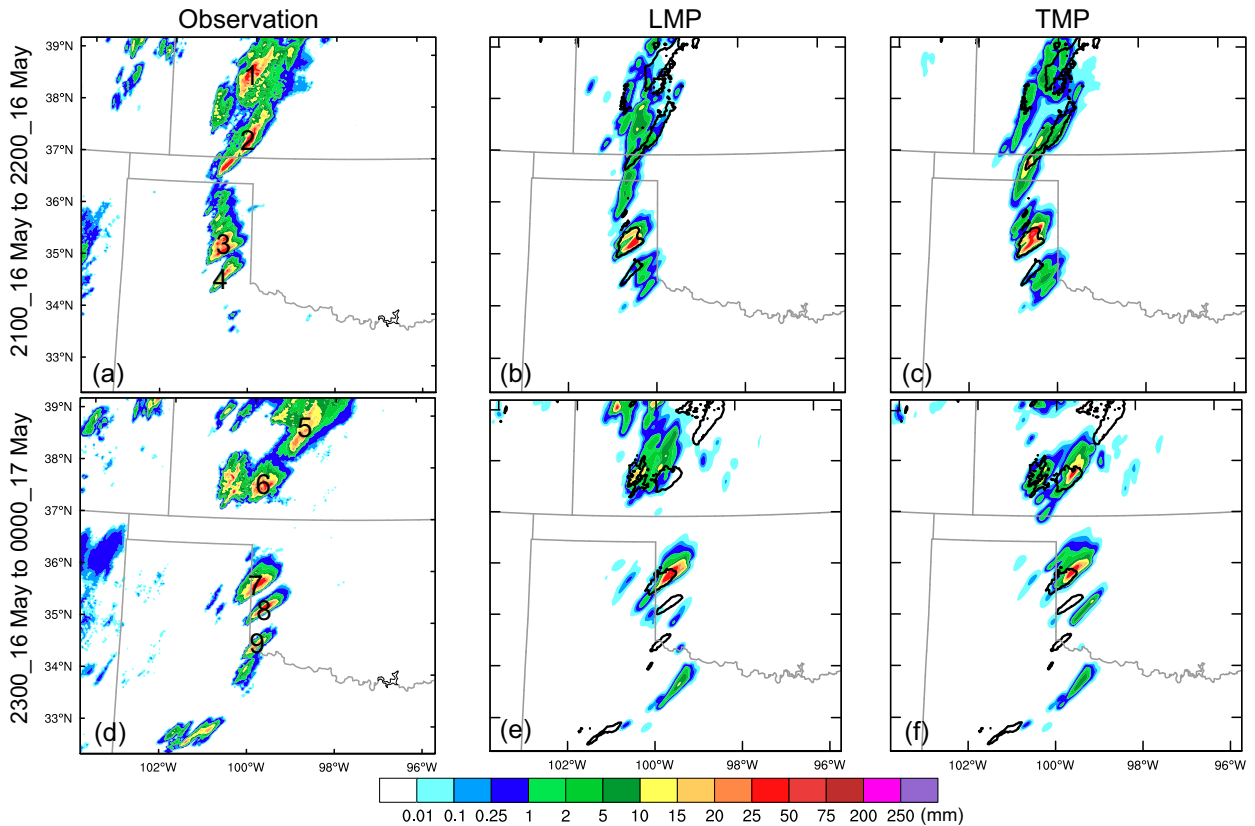
FIG. 13. Hourly precipitation (shading, mm) ending at (top) 2200 UTC 16 May and (bottom) 0000 UTC 17 May from (left) observations, and forecasts of (middle) LMP and (right) TMP experiments. The number labels the precipitation areas mentioned in the text. Observed precipitation exceeding 10 mm is contoured in black in the forecast fields.

with more cases will give more robust results in terms of the improvement due to the use of reflectivity operator consistent with the Thompson microphysics. It should be noted that even if the impact on forecasting is relatively small, the use of

an operator that is consistent with the microphysics scheme used within the prediction model is always desirable, and at the minimum doing so will ensure that the analyzed reflectivity at the initial time of forecast is continuous in time and
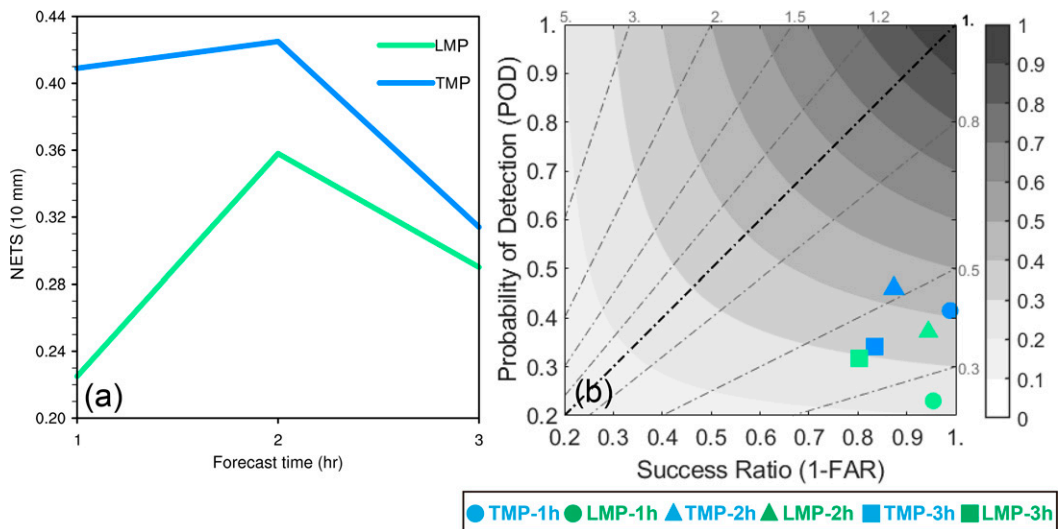

FIG. 14. (a) NETS and (b) performance diagram for hourly precipitation forecasts of LMP (green) and TMP (blue) experiments with thresholds of 10 mm. Dot, triangle, and rectangle marks in (b) represent 1-, 2-, and 3-h forecasts, respectively.
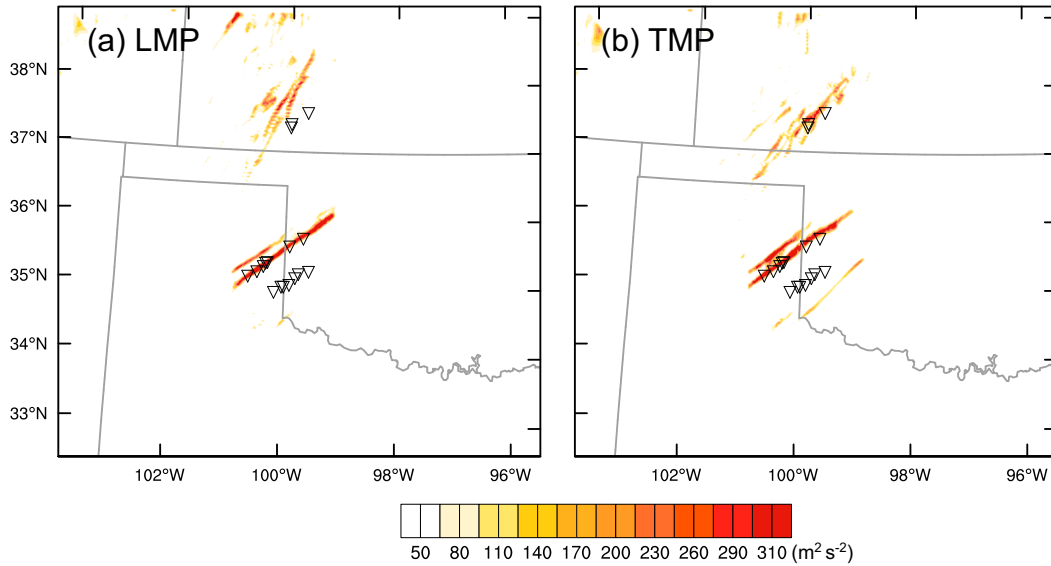
FIG. 15. The maximum 2–5-km updraft helicity tracks (shading, m^2 s^{-2}) for 0–3-h forecasts starting at 2100 UTC from the (a) LMP and (b) TMP experiments. The triangles represent tornado reports for the same period.

consistent with modeling reflectivity output right after the initial time.

As shown in this study, TMP needs more outer-loop iterations for minimization convergence than LMP because of the inclusion of N_{tr} as an additional control variable within the cost function, although the final cost function of TMP is actually smaller than that of LMP for the example examined. N_{tr} can vary by several orders of magnitude and the relationship between reflectivity and N_{tr} is highly nonlinear. Following

Chen et al. (2021), in this study, we applied a general nonlinear power transform function to the hydrometeor mixing ratios and used the transformed mixing ratios as control variables which has been shown to significantly accelerate the cost function minimization when assimilating Z data. In a separate study, we will apply the same transform function to N_{tr} and hope to achieve more efficient assimilation of radar reflectivity in the variational framework. Then, this newly developed TMP Z operator will be a promising candidate for direct
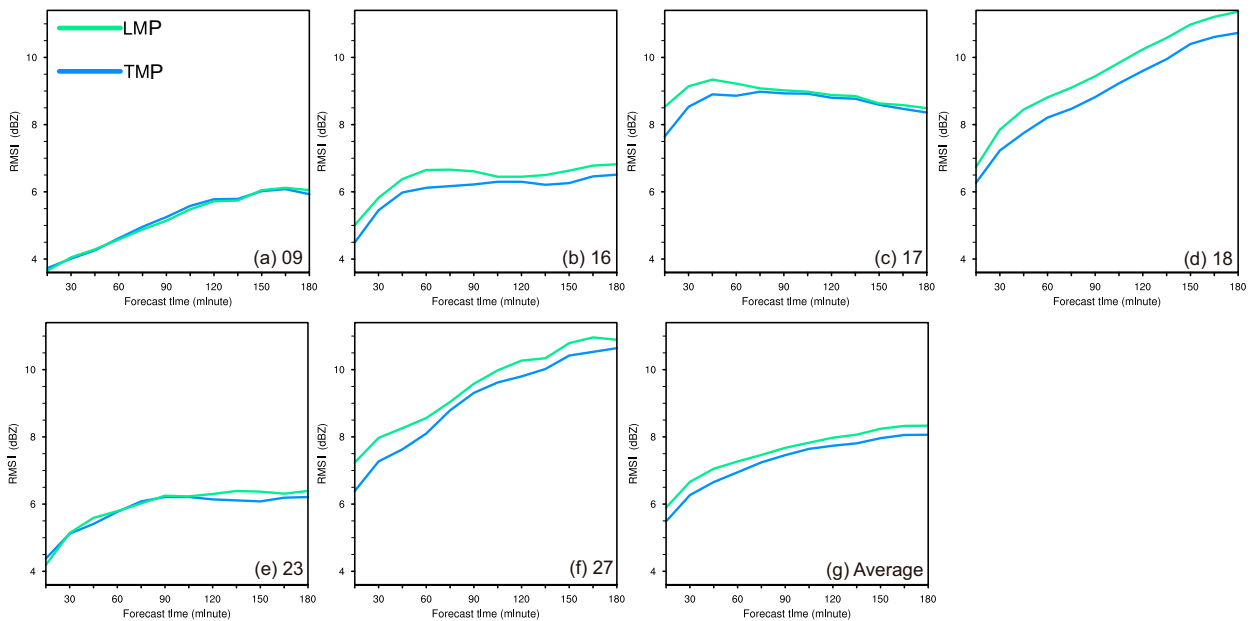

FIG. 16. RMSIs for reflectivity forecasts of LMP (green) and TMP (blue) experiments for the (a) 9, (b) 16, (c) 17, (d) 18, (e) 23, and (f) 27 May cases, and (g) the RMSIs averaged over the six cases from May 2017.
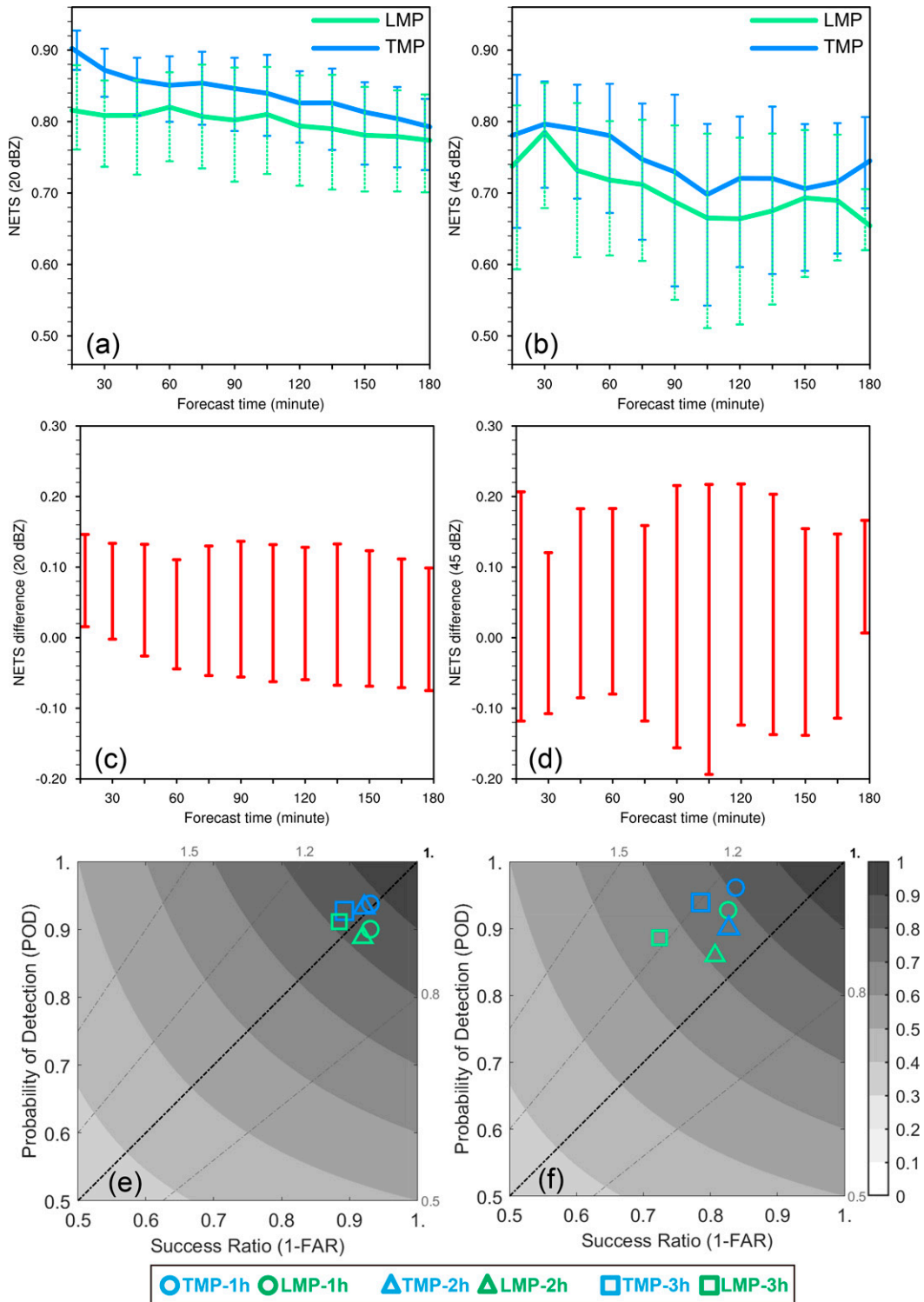
FIG. 17. (a),(b) NETS for composite reflectivity forecasts of LMP (green) and TMP (blue) experiments averaged over six cases with thresholds of (left) 20 and (right) 45 dBZ. Error bars represent the 90% confidence interval using the bootstrap resampling method. (c),(d) The 90% confidence interval of the NETS difference (TMP minus LMP). (e),(f) As in Figs. 11c and 11d, but for scores aggregated across six cases.

assimilation of radar *Z* with the EnVar method in the operational forecasting systems. Although the impacts of assimilating radar *Z* using the TMP operator on the analysis and prediction of thunderstorms over the United States are discussed in the present study, the use of the TMP *Z* operator for direct assimilation of radar *Z* can also apply to improving the forecasts for other weather systems over other regions.

REFERENCES

Alexander, C., and Coauthors, 2020: Rapid Refresh (RAP) and High Resolution Rapid Refresh (HRRR) model development. *30th Conf. on Weather Analysis and Forecasting (WAF)/26th Conf. on Numerical Weather Prediction (NWP)*, Boston, MA, Amer. Meteor. Soc., 8A.1, https://ams.confex.com/ams/2020Annual/webprogram/Paper370205.html.

Benjamin, S. G., and Coauthors, 2016: A North American hourly assimilation and model forecast cycle: The Rapid Refresh. *Mon. Wea. Rev.*, **144**, 1669–1694, https://doi.org/10.1175/MWR-D-15-0242.1.

Brewster, K., M. Hu, M. Xue, and J. Gao, 2005: Efficient assimilation of radar data at high resolution for short-range numerical weather prediction. *World Weather Research Program Symposium on Nowcasting and Very Short-Range Forecasting*, WSN05, Tolouse, France, WMP, Paper 3.06.

Carley, J., 2012: Hybrid ensemble-3DVar radar data assimilation for the short-term prediction of convective storms. Ph. D. dissertation. Department of Earth, Atmospheric, and Planetary Sciences, Purdue University, 205 pp.

Chen, F., and J. Dudhia, 2001: Coupling an advanced land surface-hydrology model with the Penn State–NCAR MM5 modeling system. Part I: Model implementation and sensitivity. *Mon. Wea. Rev.*, **129**, 569–585, https://doi.org/10.1175/1520-0493(2001)129<0569:CAALSH>2.0.CO;2.

Chen, L., C. Liu, M. Xue, G. Zhao, R. Kong, and Y. Jung, 2021: Use of power transform mixing ratios as hydrometeor control variables for direct assimilation of radar reflectivity in GSI En3DVar and tests with five convective storms cases. *Mon. Wea. Rev.*, **149**, 645–659, https://doi.org/10.1175/MWR-D-20-0149.1.

——, ——, Y. Jung, P. S. Skinner, M. Xue, and R. Kong, 2022: Object-based verification of GSI EnKF and hybrid En3DVar radar data assimilation and convection-allowing forecasts within a warn-on-forecast framework. *Wea. Forecasting*, in press, https://doi.org/10.1175/WAF-D-20-0180.1.

Clark, A. J., W. A. Gallus, and M. L. Weisman, 2010: Neighborhood-based verification of precipitation forecasts from convection-allowing NCAR WRF Model simulations and the operational NAM. *Wea. Forecasting*, **25**, 1495–1509, https://doi.org/10.1175/2010WAF2222404.1.

——, J. S. Kain, P. T. Marsh, J. Correia, M. Xue, and F. Y. Kong, 2012: Forecasting tornado pathlengths using a three-dimensional object identification algorithm applied to convection-allowing forecasts. *Wea. Forecasting*, **27**, 1090–1113, https://doi.org/10.1175/WAF-D-11-00147.1.

Courtier, P., J.-N. Thépaut, and A. Hollingsworth, 1994: A strategy for operational implementation of 4D-Var, using an incremental approach. *Quart. J. Roy. Meteor. Soc.*, **120**, 1367–1387, https://doi.org/10.1002/qj.49712051912.

Dawson, D. T., M. Xue, J. A. Milbrandt, and M. K. Yau, 2010: Comparison of evaporation and cold pool development between single-moment and multimoment bulk microphysics schemes in idealized simulations of tornadic thunderstorms. *Mon. Wea. Rev.*, **138**, 1152–1171, https://doi.org/10.1175/2009MWR2956.1.

Dowell, D., L. J. Wicker, and C. Snyder, 2011: Ensemble Kalman filter assimilation of radar observations of the 8 May 2003 Oklahoma City supercell: Influence of reflectivity observations on storm-scale analysis. *Mon. Wea. Rev.*, **138**, 1152–1171, https://doi.org/10.1175/2010MWR3438.1.

——, and Coauthors, 2016: Development of a High-Resolution Rapid Refresh Ensemble (HRRRE) for severe weather forecasting. *28th Conf. on Severe Local Storms*, Portland, OR, Amer. Meteor. Soc., 8B.2., https://ams.confex.com/ams/28SLS/webprogram/Paper301555.html.

Duda, J. D., X. Wang, Y. Wang, and J. R. Carley, 2019: Comparing the assimilation of radar reflectivity using the direct GSI-based Ensemble–Variational (EnVar) and indirect cloud analysis methods in convection-allowing forecasts over the continental United States. *Mon. Wea. Rev.*, **147**, 1655–1678, https://doi.org/10.1175/MWR-D-18-0171.1.

Evensen, G., 2003: The ensemble Kalman filter: Theoretical formulation and practical implementation. *Ocean Dyn.*, **53**, 343–367, https://doi.org/10.1007/s10236-003-0036-9.

Gao, J., 2014: Some observing system simulation experiments with a hybrid 3DEnVAR system for storm-scale radar data assimilation. *Mon. Wea. Rev.*, **142**, 3326–3346, https://doi.org/10.1175/MWR-D-14-00025.1.

——, and D. J. Stensrud, 2012a: Assimilation of reflectivity data in a convective-scale, cycled 3DVAR framework with hydrometeor classification. *J. Atmos. Sci.*, **69**, 1054–1065, https://doi.org/10.1175/JAS-D-11-0162.1.

——, and ——, 2012b: Assimilation of reflectivity data in a convective-scale, cycled 3DVAR framework with hydrometeor classification. *J. Atmos. Sci.*, **69**, 1054–1065, https://doi.org/10.1175/JAS-D-11-0162.1.

Gilmore, M. S., J. M. Straka, and E. N. Rasmussen, 2004: Precipitation uncertainty due to variations in precipitation particle parameters within a simple microphysics scheme. *Mon. Wea. Rev.*, **132**, 2610–2627, https://doi.org/10.1175/MWR2810.1.

Hamill, T. M., J. S. Whitaker, D. T. Kleist, M. Fiorino, and S. G. Benjamin, 2011: Predictions of 2010's tropical cyclones using the GFS and ensemble-based data assimilation methods. *Mon. Wea. Rev.*, **139**, 3243–3247, https://doi.org/10.1175/MWR-D-11-00079.1.

Hong, S., and J.-O. J. Lim, 2006: The WRF single-moment 6-class microphysics scheme (WSM6). *J. Korean Meteor. Soc.*, **42**, 129–151.

——, Y. Noh, and J. Dudhia, 2006: A new vertical diffusion package with an explicit treatment of entrainment processes. *Mon. Wea. Rev.*, **134**, 2318–2341, https://doi.org/10.1175/MWR3199.1.

Hu, M., M. Xue, and K. Brewster, 2006: 3DVAR and cloud analysis with WSR-88D level-II data for the prediction of the Fort Worth, Texas, tornadic thunderstorms. Part I: Cloud analysis and its impact. *Mon. Wea. Rev.*, **134**, 675–698, https://doi.org/10.1175/MWR3092.1.

——, S. G. Benjamin, T. T. Ladwig, D. C. Dowell, S. S. Weygandt, C. R. Alexander, and J. S. Whitaker, 2017: GSI three-dimensional ensemble–variational hybrid data assimilation using a global ensemble for the regional Rapid Refresh model. *Mon. Wea. Rev.*, **145**, 4205–4225, https://doi.org/10.1175/MWR-D-16-0418.1.

Iacono, M. J., J. S. Delamere, E. J. Mlawer, M. W. Shephard, S. A. Clough, and W. D. Collins, 2008: Radiative forcing by long-lived greenhouse gases: Calculations with the AER radiative transfer models. *J. Geophys. Res.*, **113**, D13103, https://doi.org/10.1029/2008JD009944.

Jankov, I., J. Beck, J. Wolff, M. Harrold, J. B. Olson, T. Smirnova, C. Alexander, and J. Berner, 2019: Stochastically perturbed parameterizations in an HRRR-based ensemble. *Mon. Wea. Rev.*, **147**, 153–173, https://doi.org/10.1175/MWR-D-18-0092.1.

Johnson, M., Y. Jung, D. T. Dawson, and M. Xue, 2016: Comparison of simulated polarimetric signatures in idealized supercell storms using two-moment bulk microphysics schemes in WRF. *Mon. Wea. Rev.*, **144**, 971–996, https://doi.org/10.1175/MWR-D-15-0233.1.

Jung, Y., G. Zhang, and M. Xue, 2008: Assimilation of simulated polarimetric radar data for a convective storm using the ensemble Kalman filter. Part I: Observation operators for reflectivity and polarimetric variables. *Mon. Wea. Rev.*, **136**, 2228–2245, https://doi.org/10.1175/2007MWR2083.1.

——, M. Xue, and G. Zhang, 2010: Simulations of polarimetric radar signatures of a supercell storm using a two-moment bulk microphysics scheme. *J. Appl. Meteor. Climatol.*, **49**, 146–163, https://doi.org/10.1175/2009JAMC2178.1.

——, ——, and M. Tong, 2012: Ensemble Kalman filter analyses of the 29–30 May 2004 Oklahoma tornadic thunderstorm using one- and two-moment bulk microphysics schemes, with verification against polarimetric data. *Mon. Wea. Rev.*, **140**, 1457–1475, https://doi.org/10.1175/MWR-D-11-00032.1.

Kain, J. S., S. J. Weiss, J. J. Levit, M. E. Baldwin, and D. R. Bright, 2006: Examination of convection-allowing configurations of the WRF Model for the prediction of severe convective weather: The SPC/NSSL spring program 2004. *Wea. Forecasting*, **21**, 167–181, https://doi.org/10.1175/WAF906.1.

——, and Coauthors, 2008: Some practical considerations for the first generation of operational convection-allowing NWP: How much resolution is enough? *Wea. Forecasting*, **23**, 931–952, https://doi.org/10.1175/WAF2007106.1.

Kessler, E., 1995: On the continuity and distribution of water substance in atmospheric circulations. *Atmos. Res.*, **38**, 109–145, https://doi.org/10.1016/0169-8095(94)00090-Z.

Kleist, D. T., D. F. Parrish, J. C. Derber, R. Treadon, W.-S. Wu, and S. Lord, 2009: Introduction of the GSI into the NCEP global data assimilation system. *Wea. Forecasting*, **24**, 1691–1705, https://doi.org/10.1175/2009WAF2222201.1.

Kong, R., M. Xue, and C. S. Liu, 2018: Development of a hybrid En3DVar data assimilation system and comparisons with 3DVar and EnKF for radar data assimilation with observing system simulation experiments. *Mon. Wea. Rev.*, **146**, 175–198, https://doi.org/10.1175/MWR-D-17-0164.1.

Labriola, J., N. Snook, Y. Jung, B. Putnam, and M. Xue, 2017: Ensemble hail prediction for the storms of 10 May 2010 in south-central Oklahoma using single- and double-moment microphysical schemes. *Mon. Wea. Rev.*, **145**, 4911–4936, https://doi.org/10.1175/MWR-D-17-0039.1.

——, ——, ——, and M. Xue, 2020: Evaluating ensemble Kalman filter analyses of severe hail storms on 8 May 2017 in Colorado: Effects of state variable updating and multi-moment microphysics schemes on state variable cross-covariances. *Mon. Wea. Rev.*, **148**, 2365–2389, https://doi.org/10.1175/MWR-D-19-0300.1.

——, Y. Jung, L. Chengsi, and M. Xue, 2021: Evaluating forecast performance and sensitivity to the GSI EnKF data assimilation configuration for the 28–29 May 2017 mesoscale convective system case. *Wea. Forecasting*, **36**, 127–146, https://doi.org/10.1175/WAF-D-20-0071.1.

Lin, Y.-L., R. D. Farley, and H. D. Orville, 1983: Bulk parameterization of the snow field in a cloud model. *J. Climate Appl. Meteor.*, **22**, 1065–1092, https://doi.org/10.1175/1520-0450(1983)022<1065:BPOTSF>2.0.CO;2.

Liu, C., M. Xue, and R. Kong, 2020: Direct variational assimilation of radar reflectivity and radial velocity data: Issues with nonlinear reflectivity operator and solutions. *Mon. Wea. Rev.*, **148**, 1483–1502, https://doi.org/10.1175/MWR-D-19-0149.1.

Liu, H., and M. Xue, 2008: Prediction of convective initiation and storm evolution on 12 June 2002 during IHOP_2002. Part I: Control simulation and sensitivity experiments. *Mon. Wea. Rev.*, **136**, 2261–2282, https://doi.org/10.1175/2007MWR2161.1.

Luo, L., 2018: Explicit prediction of hail in a long-lasting multicellular convective system in eastern China using multi-moment microphysics schemes. *J. Atmos. Sci.*, **75**, 3115–3137, https://doi.org/10.1175/JAS-D-17-0302.1.

——, M. Xue, K. Zhu, and B. Zhou, 2017: Explicit prediction of hail in a hailstorm of 19 March 2014 in eastern China using multi-moment microphysics schemes. *J. Geophys. Res. Atmos.*, **122**, 7560–7581, https://doi.org/10.1002/2017JD026747.

Marshall, J. S., and W. M. Palmer, 1948: The distribution of raindrops with size. *J. Meteor.*, **5**, 165–166, https://doi.org/10.1175/1520-0469(1948)005<0165:TDORWS>2.0.CO;2.

Milbrandt, J. A., and M. K. Yau, 2005a: A multimoment bulk microphysics parameterization. Part I: Analysis of the role of the spectral shape parameter. *J. Atmos. Sci.*, **62**, 3051–3064, https://doi.org/10.1175/JAS3534.1.

——, and ——, 2005b: A multimoment bulk microphysics parameterization. Part II: A proposed three-moment closure and scheme description. *J. Atmos. Sci.*, **62**, 3065–3081, https://doi.org/10.1175/JAS3535.1.

Pan, Y., K. Zhu, M. Xue, X. Wang, M. Hu, S. G. Benjamin, S. S. Weygandt, and J. S. Whitaker, 2014: A GSI-based coupled EnSRF–En3DVar hybrid data assimilation system for the operational Rapid Refresh model: Tests at a reduced resolution. *Mon. Wea. Rev.*, **142**, 3756–3780, https://doi.org/10.1175/MWR-D-13-00242.1.

Putman, W. M., and S. J. Lin, 2007: Finite-volume transport on various cubed-sphere grids. *J. Comput. Phys.*, **227**, 55–78, https://doi.org/10.1016/j.jcp.2007.07.022.

Putnam, B. J., M. Xue, Y. S. Jung, N. Snook, and G. F. Zhang, 2014: The analysis and prediction of microphysical states and polarimetric radar variables in a mesoscale convective system using double-moment microphysics, multinetwork radar data, and the ensemble Kalman filter. *Mon. Wea. Rev.*, **142**, 141–162, https://doi.org/10.1175/MWR-D-13-00042.1.

Roebber, P. J., 2009: Visualizing multiple measures of forecast quality. *Wea. Forecasting*, **24**, 601–608, https://doi.org/10.1175/2008WAF2222159.1.

Skamarock, W. C., J. B. Klemp, J. Dudhia, D. O. Gill, D. M. Barker, W. Wang, and J. G. Powers, 2005: A description of the Advanced Research WRF version 2. NCAR Tech. Note NCAR/TN-468+STR, 88 pp., https://doi.org/10.5065/D6DZ069T.

Skinner, P. S., and Coauthors, 2018: Object-based verification of a prototype Warn-on-Forecast system. *Wea. Forecasting*, **33**, 1225–1250, https://doi.org/10.1175/WAF-D-18-0020.1.

Smith, P. L., Jr., C. G. Myers, and H. D. Orville, 1975: Radar reflectivity factor calculations in numerical cloud models using bulk parameterization of precipitation processes. *J. Appl. Meteor.*, **14**, 1156–1165, https://doi.org/10.1175/1520-0450(1975)014<1156:RRFCIN>2.0.CO;2.

Smith, T. L., S. G. Benjamin, J. M. Brown, S. S. Weygandt, T. Smirnova, and B. Schwartz, 2008: Convection forecasts from the hourly updated, 3-km High Resolution Rapid Refresh (HRRR) model. *24th Conf. on Severe Local Storms*, Savannah, GA, Amer. Meteor. Soc., 11.1, https://ams.confex.com/ams/24SLS/techprogram/paper_142055.htm.

Smith, T. M., and Coauthors, 2016: Multi-Radar Multi-Sensor (MRMS) severe weather and aviation products: Initial operating capabilities. *Bull. Amer. Meteor. Soc.*, **97**, 1617–1630, https://doi.org/10.1175/BAMS-D-14-00173.1.

Snook, N., and M. Xue, 2008: Effects of microphysical drop size distribution on tornadogenesis in supercell thunderstorms. *Geophys. Res. Lett.*, **35**, L24803, https://doi.org/10.1029/2008GL035866.

——, ——, and A. D. Schenkman, 2008: Assimilation of CASA radar data for a tornadic convective system using ensemble Kalman filters. *Symp. on Recent Developments in Atmospheric Applications of Radar and Lidar*, New Orleans, LA, Amer. Meteor. Soc., P2.19, https://ams.confex.com/ams/88Annual/techprogram/paper_134263.htm.

Stensrud, D. J., and Coauthors, 2009: Convective-scale Warn-on-Forecast system: A vision for 2020. *Bull. Amer. Meteor. Soc.*, **90**, 1487–1500, https://doi.org/10.1175/2009BAMS2795.1.

Sun, J., and N. A. Crook, 1997: Dynamical and microphysical retrieval from Doppler radar observations using a cloud model and its adjoint. Part I: Model development and simulated data experiments. *J. Atmos. Sci.*, **54**, 1642–1661, https://doi.org/10.1175/1520-0469(1997)054<1642:DAMRFD>2.0.CO;2.

Tallapragada, V., C. Kieu, Y. Kwon, S. Trahan, Q. Liu, Z. Zhang, and I.-H. Kwon, 2014: Evaluation of storm structure from the operational HWRF during 2012 implementation. *Mon. Wea. Rev.*, **142**, 4308–4325, https://doi.org/10.1175/MWR-D-13-00010.1.

Tao, W.-K., and Coauthors, 2003: Microphysics, radiation and surface processes in the Goddard Cumulus Ensemble (GCE) model. *Meteor. Atmos. Phys.*, **82**, 97–137, https://doi.org/10.1007/s00703-001-0594-7.

Thompson, G., R. M. Rasmussen, and K. Manning, 2004: Explicit forecasts of winter precipitation using an improved bulk microphysics scheme. Part I: Description and sensitivity

analysis. *Mon. Wea. Rev.*, **132**, 519–542, https://doi.org/10.1175/1520-0493(2004)132<0519:EFOWPU>2.0.CO;2.

——, P. R. Field, R. M. Rasmussen, and W. D. Hall, 2008: Explicit forecasts of winter precipitation using an improved bulk microphysics scheme. Part II: Implementation of a new snow parameterization. *Mon. Wea. Rev.*, **136**, 5095–5115, https://doi.org/10.1175/2008MWR2387.1.

Tong, C.-C., Y. Jung, M. Xue, and C. Liu, 2020: Direct assimilation of radar data with ensemble Kalman filter and hybrid ensemble-variational method in the National Weather Service operational data assimilation system GSI for the stand-alone regional FV3 model at a convection-allowing resolution. *Geophy. Res. Lett.*, **47**, e2020GL090179, https://doi.org/10.1029/2020GL090179.

Tong, M., and M. Xue, 2005: Ensemble Kalman filter assimilation of Doppler radar data with a compressible nonhydrostatic model: OSS experiments. *Mon. Wea. Rev.*, **133**, 1789–1807, https://doi.org/10.1175/MWR2898.1.

——, and ——, 2008: Simultaneous estimation of microphysical parameters and atmospheric state with radar data and ensemble square-root Kalman filter. Part II: Parameter estimation experiments. *Mon. Wea. Rev.*, **136**, 1649–1668, https://doi.org/10.1175/2007MWR2071.1.

Ulbrich, C. W., 1983: Natural variations in the analytical form of the raindrop size distributions. *J. Climate Appl. Meteor.*, **22**, 1764–1775, https://doi.org/10.1175/1520-0450(1983)022<1764:NVITAF>2.0.CO;2.

Wang, Y., and X. Wang, 2017: Direct assimilation of radar reflectivity without tangent linear and adjoint of the nonlinear observation operator in the GSI-based EnVar system: Methodology and experiment with the 8 May 2003 Oklahoma City tornadic supercell. *Mon. Wea. Rev.*, **145**, 1447–1471, https://doi.org/10.1175/MWR-D-16-0231.1.

——, J. Gao, P. S. Skinner, K. Knopfmeier, T. Jones, G. Creager, P. L. Heiselman, and L. J. Wicker, 2019: Test of a weather-adaptive dual-resolution hybrid Warn-on-Forecast analysis and forecast system for several severe weather events. *Wea. Forecasting*, **34**, 1807–1827, https://doi.org/10.1175/WAF-D-19-0071.1.

Wheatley, D. M., K. H. Knopfmeier, T. A. Jones, and G. J. Creager, 2015: Storm-scale data assimilation and ensemble forecasting with the NSSL experimental Warn-on-Forecast system. Part I: Radar data experiments. *Wea. Forecasting*, **30**, 1795–1817, https://doi.org/10.1175/WAF-D-15-0043.1.

Wu, W.-S., D. F. Parrish, E. Rogers, and Y. Lin, 2016: Regional ensemble–variational data assimilation using global ensemble forecasts. *Wea. Forecasting*, **32**, 83–96, https://doi.org/10.1175/WAF-D-16-0045.1.

Xue, M., and Coauthors, 2001: The Advanced Regional Prediction System (ARPS)—A multi-scale nonhydrostatic atmospheric simulation and prediction tool. Part II: Model physics and applications. *Meteor. Atmos. Phys.*, **76**, 143–165, https://doi.org/10.1007/s007030170027.

——, D. Wang, J. Gao, K. Brewster, and K. K. Droegemeier, 2003: The Advanced Regional Prediction System (ARPS), storm-scale numerical weather prediction and data assimilation. *Meteor. Atmos. Phys.*, **82**, 139–170, https://doi.org/10.1007/s00703-001-0595-6.

——, Y. Jung, and G. Zhang, 2010: State estimation of convective storms with a two-moment microphysics scheme and an ensemble Kalman filter: Experiments with simulated radar data. *Quart. J. Roy. Meteor. Soc.*, **136**, 685–700, https://doi.org/10.1002/qj.593.

——, J. Schleif, F. Kong, K. W. Thomas, Y. Wang, and K. Zhu, 2013: Track and intensity forecasting of hurricanes: Impact of convection-permitting resolution and global ensemble Kalman filter analysis on 2010 Atlantic season forecasts. *Wea. Forecasting*, **28**, 1366–1384, https://doi.org/10.1175/WAF-D-12-00063.1.

Yussouf, N., E. R. Mansell, L. J. Wicker, D. M. Wheatley, and D. J. Stensrud, 2013: The ensemble Kalman filter analyses and forecasts of the 8 May 2003 Oklahoma City tornadic supercell storm using single- and double-moment microphysics schemes. *Mon. Wea. Rev.*, **141**, 3388–3412, https://doi.org/10.1175/MWR-D-12-00237.1.